DOI: https://doi.org/10.2138/am-2018-6225

REVISION 1:Ascent rates of rhyolitic magma at the onset of three caldera-forming eruptions

Madison L. Myers[1,*], Paul J. Wallace[1], Colin J.N. Wilson[2], James M. Watkins[1], and Yang Liu[3]

[1] Department of Earth Sciences, University of Oregon, Eugene, OR 97403-1272, USA
[2] School of Geography, Environment and Earth Sciences, Victoria University, PO Box 600, Wellington 6140, New Zealand
[3] Jet Propulsion Laboratory, California Institute of Technology, Pasadena, California 91109, USA.

*Corresponding author. Email address: mmyers3@uoregon.edu

ABSTRACT

Important clues to the initiation and early behavior of large (super-) eruptions lie in the records of degassing during magma ascent. Here we investigate the timescales of magma ascent for three rhyolitic supereruptions that show field evidence for contrasting behavior at eruption onset: (1) 650 km^3, 0.767 Ma Bishop Tuff, Long Valley, (2) 530 km^3, 25.4 ka Oruanui eruption, Taupo, and (3) 2,500 km^3, 2.08 Ma Huckleberry Ridge Tuff, Yellowstone. During magma ascent, decompression causes volatile exsolution from the host melt into bubbles, leading to H_2O and CO_2 gradients in quartz-hosted reentrants (REs; unsealed inclusions). These gradients are modeled to estimate ascent rates. We present best-fit modeled ascent rates for H_2O and CO_2 profiles for REs in early-erupted fall deposits from Bishop (n = 13), Oruanui (n = 9) and Huckleberry Ridge (n = 9). Using a Matlab script that includes an error minimization function, Bishop REs yield ascent rates of 0.6-13 m/s, overlapping with and extending beyond those of the Huckleberry Ridge (0.3-4.0 m/s). Reentrants in Oruanui quartz crystals from the first two eruptive phases (of ten) yield the slowest ascent rates determined in this study (0.06-0.2 m/s), whereas those from phase three, which has clear field evidence for a marked increase in eruption intensity, are uniformly higher (1.4-2.6 m/s).

For all three eruptions, the interiors of most REs appear to have re-equilibrated to lower H_2O and CO_2 concentrations when compared to co-erupted, enclosed melt inclusions in quartz. Such reequilibration implies the presence of an initial period of slower ascent, likely resulting from movement of magma from storage into a developing conduit system, prior to the faster (<1-2.5 hours) final ascent of magma to the surface. This slower initial movement represents hours to several days of reequilibration, invalidating any assumption of constant decompression conditions from the storage region. However, the number of REs with deeper starting depths increases with stratigraphic height in all three deposits (particularly the Bishop Tuff), suggesting progressive elimination of the deep, sluggish ascent stage over time, which we interpret to be the result of maturing of the conduit system(s). Our results agree well with ascent rates estimated using theoretical approximations and numerical modeling for plinian rhyolitic eruptions (0.7-30 m/s), but overlap more with the slower estimates.

INTRODUCTION

Magma ascent rates

The rate at which magma ascends has a strong influence on the manner in which it (eventually) erupts. Slower ascent allows degassing of volatiles from the magma, favoring a more effusive eruption, whereas fast decompression fosters volatile retention and consequently results in more explosive behavior (Eichelberger et al. 1986; Mangan and Sisson 2000; Cashman 2004; Castro and Gardner 2008). Determining the rates at which magma ascends, and how those rates evolve over the course of an eruption, is thus important for understanding eruptive activity and improving monitoring and response for specific volcanoes (Dingwell 1996). Furthermore, the ability to determine ascent rates through the use of erupted materials permits reconstruction of the progression of activity from individual eruptions, including historic events.

Ascent rates have been estimated using experimentally determined rates of breakdown rim formation on hydrous phases, the growth of microlites in matrix melt, and bubble number densities (see review in Rutherford 2008). However, many of these methods are best applied to slower magma ascents, hotter systems with lower silica contents, or are heavily influenced by processes in specific regions of the conduit system (e.g. bubbles nucleating around the fragmentation front; Toramaru 2006; Rotella et al. 2014). For large explosive rhyolitic eruptions, ascent timescales are often so short that they remain difficult to constrain with petrological tools. As a result, many studies have used analytical and numerical conduit models to constrain values (5-30 m/s: see reviews by Rutherford 2008; Gonnermann and Manga 2013), or used estimates based on the diffusion rate of H_2O into bubbles (0.7-5 m/s: summarized in Rutherford 2008). Thus, our ability to determine magma ascent rates for explosive rhyolitic eruptions requires the application of a speedometer that can record short timescales and be quenched rapidly after fragmentation.

Several recent studies have exploited volatile exsolution in response to decompression during magma ascent to estimate ascent rates (Liu et al. 2007; Humphreys et al. 2008; Lloyd et al. 2014; Myers et al. 2016; Ferguson et al. 2016). Melt-filled reentrants (REs; also commonly referred to as embayments) in phenocryst minerals are not sealed by crystal growth and therefore can record late-stage changes in the melt surrounding the host crystal. Such changes of particular interest here are those resulting in gradients in H_2O and CO_2 (and in more mafic examples, S) in the REs that can be modeled to estimate ascent timescales (Liu et al. 2007; Humphreys et al. 2008; Lloyd et al. 2014; Myers et al. 2016; Ferguson et al. 2016). Because pressure-dependent solubilities are well-known and precise measurements of H_2O and CO_2 concentrations can be made, modeling of volatile profiles in REs presents a powerful tool for constraining ascent timescales for individual eruptions (Liu et al. 2007).

The use of REs has advanced in the past decade from diffusion modeling of 1-2 single H_2O and CO_2 point analyses (Oruanui: Liu et al. 2007; n = 9) and H_2O grayscale calibrated transects using electron microprobe analyses (Mount St. Helens: Humphreys et al. 2008; n = 3), to high-precision NanoSIMs H_2O and CO_2 transects (Fuego; Lloyd et al. 2014, n = 4; Ferguson et al. 2016, n = 4). Here we use concentration profiles for H_2O and CO_2 determined by Fourier Transform Infrared Spectroscopy for 38 reentrants in quartz and present best-fit diffusion profiles calculated using a decompression model for 31 of them. We focus on samples from the fall deposits of three rhyolitic supereruptions for which extensive fieldwork has been previously conducted, providing a solid framework for integrating calculated ascent rates with inferred eruption dynamics. Our study is motivated by a desire to understand: (1) whether decompression rates increase with increases in eruption intensity inferred from field studies; (2) how ascent rates evolve over the course of an eruption; and (3) whether ascent rates can be related to inferred vent geometry, including the shift into the caldera-forming stages of the eruptions.

Geologic background

We investigated three voluminous, caldera-forming eruptions in this study (Fig. 1).

1. The Bishop Tuff, Long Valley, California (650 km^3 magma, 0.767 Ma), where early fall activity graded continuously into climactic eruption (Wilson and Hildreth 1997).
2. The Oruanui eruption, Taupo, New Zealand (530 km^3 magma, 25.4 ka), which experienced a time break of months between the first outbreak and subsequent activity (Wilson 2001)
3. The Huckleberry Ridge Tuff, Yellowstone (2,500 km^3 magma, 2.08 Ma) where the initial activity was prolonged and episodic over days to weeks (Myers et al. 2016; Wilson et al. in preparation).

Aside from the contrasts in initial behavior, both the Bishop and Oruanui eruptions exhibit a marked transition, inferred from field evidence, from a single-vent configuration to multiple vents related with caldera formation. Because the corresponding transition in the Huckleberry Ridge Tuff is associated with deposition of hot ignimbrite and has no associated rapidly quenched fall material, no ascent rates could be constrained for the caldera-forming phase of this eruption.

In the Bishop eruption, deposition of fall material and onset into coeval flow activity is inferred to have been a continuous process. The transition from a single vent to multiple vents is documented from lithic evidence (Hildreth and Mahood 1986), with the incoming of fragments from the older Glass Mountain complex near the top of fall unit F8 (Wilson and Hildreth 1997), indicating development of vents around the caldera ring fracture (Fig. 1). However, caldera collapse very likely began earlier, as roughly 2/3 of the erupted volume had already been discharged by this stage (Hildreth and Wilson 2007). Importantly, there is no field evidence for significant depositional breaks (more than a few hours) inferred from any of the Bishop Tuff deposits.

In contrast, the Oruanui supereruption can be subdivided based upon layering in its fall deposits into ten phases, with time breaks inferred between five of these phases (Wilson 2001). The most significant time break, of weeks to months, lies between the activity of phases one and two, where significant reworking and bioturbation of the earlier fall layer is observed (Wilson 2001). These two phases also involve co-venting of 'foreign' biotite-bearing pumices (3%-16% of sampled 16-32 mm pumices) sourced from an independent magmatic system 10-15 km away (Allan et al. 2012). The presence of this laterally-injected magma suggests that these phases were controlled through rifting processes permitting diking to occur along regional faults (Allan et al. 2012). The transition to caldera formation is piecemeal, however, probably starting in Phase 3, with a marked escalation in the volume, discharge rate and dispersal power of the eruption.

Deposits of the Huckleberry Ridge eruption are three voluminous ignimbrite members (A, B and C), with initial pre-A and later pre-C fall deposits (Christiansen 2001). The initial (pre-A) fall deposits studied for this paper preserve evidence in their lower parts for small-scale reworking, suggesting short breaks in deposition during the opening eruption stages (Myers et al. 2016; Wilson 2009 and manuscript in preparation). Support for this episodic eruption onset comes also from scatter in measured H_2O concentrations in enclosed melt inclusions, observed in multiple layers through the fall deposit and interpreted to reflect slow ascent (days to weeks) of the first-erupted magma (Myers et al. 2016). In addition, the geochemical clustering of melt inclusion, obsidian pyroclast, and matrix glass compositions throughout the fall deposit suggests that multiple vent systems were simultaneously active and co-depositing tephra, tapping three distinct magma domains at the top of the major magma body (Myers et al. 2016).

ANALYTICAL METHODS

Whole pumice clasts were sampled where possible from individual layers (linked to published stratigraphies for the Bishop and Oruanui) through each fall deposit (Fig. 1). Where the grain size was too fine for individual pumices to be sampled (e.g., early Bishop, Huckleberry Ridge), glass-coated loose crystals were separated from samples of bulk fall material from distinct stratigraphic horizons. Nine horizons were sampled in each of the Huckleberry Ridge and Bishop fall deposits, and three in the Oruanui eruption, although not all sampled layers contained useable REs (see details in Table 1). Samples were crushed (when necessary), sieved to 500-1000 μm and picked for whole, glass-coated quartz crystals. Quartz crystals were then immersed in isopropyl alcohol to aid in visual inspection under a binocular microscope. Crystals were chosen for this study that contained a RE >100 μm in length that preserved a simple morphology, that is, a rectilinear shape with a wide mouth and lacking internal bends (Fig. 2, Supplementary Fig. 1). Selected crystals were individually mounted in crystal bond and carefully positioned to insure intersection of the entire length of the RE (Fig. 2b,c). The crystals were then ground and polished to doubly expose the RE, with only those REs preserving inner and rim glass being used for analysis. Quartz-hosted melt inclusions (MIs) from the same horizons and clasts from which REs were chosen were separately mounted for analysis.

Water and CO_2 concentration maps and transects with a spatial resolution of ~20-25 μm were measured using a Thermo Nicolet Nexus 670 Fourier Transform Infrared (FTIR) spectrometer interfaced with a Continuum IR microscope at the University of Oregon using a computer-controlled stage. Measured absorbance peak heights were converted to H_2O and CO_2 concentrations using the Beer-Lambert law ($c_i = M_i \cdot A/\rho \cdot d \cdot \varepsilon$). In this equation, c_i is the concentration of the absorbing species, M_i is the molecular weight of the species (g/mol), A is the absorbance (peak height) of the relevant vibration band, ρ is the glass density (g/L), d is the thickness of the wafer analyzed (cm) and ε is the molar absorption coefficient (L/mol·cm). Total H_2O concentration was calculated using the 3550 cm^{-1} peak. In rhyolitic compositions, ρ and ε strongly depend on total H_2O concentration. This requires the use of an iterative process to converge on appropriate values [Eq. 1 (Skirius, 1990) and Eq. 2 (Leschik et al., 2004)]:

$$\rho = 2350 - 12.6\, C_{H_2O} \quad \text{Eq. 1}$$

$$\varepsilon = 80 - 1.36\, C_{H_2O} \quad \text{Eq. 2,}$$

where C_{H_2O} is the concentration of total dissolved H_2O in wt% measured from each analytical spot. The absorption coefficient (ε) for molecular CO_2 (2350 cm^{-1}) in rhyolitic glass is 1214 L/mol·cm (Behrens et al., 2004). Thicknesses were measured using both a digital micrometer (±2 μm) and the reflectance interference fringe method (Wysoczanski and Tani 2006), which allows for specific locations within the grain (e.g. interior vs. rim of each reentrant) to be measured. All H_2O and CO_2 profile concentrations and distances from rim can be found in Online Supplementary Table 1.

After FTIR analysis, quartz wafers were set in a 1-inch epoxy mount for analysis of major elements using a Cameca SX-100 electron microprobe (EPMA) at the University of Oregon. Operating conditions were 15 kV and 10 nA sample current for Si, Ca, Na, Fe, Al, and K, and 50 nA current for Cl, F, Mg and Ti. A 10 µm defocused beam was used for all analyses. Sodium, K, Si, and Al were measured first, and their concentrations were calculated using a time-dependent intensity correction in Probe for Windows (Donovan et al. 2007**)**. Glasses were then analyzed for trace elements by Laser-Ablation Inductively Coupled Plasma Mass Spectrometry (LA-ICP-MS) at Oregon State University using a 50-µm spot size, with four glass standards (GSE-1G, BHVO, ANTO, and BCR) for secondary calibration, ^{29}Si as an internal standard, and GSE-1G as a check standard throughout the run. Reentrant volatile, major and trace element data can be found in Supplementary Table 2. The full MI dataset, which we use below for comparison with the REs, is presented in Myers (2017).

RESULTS

All quartz-hosted reentrants (RE) from the Bishop and Oruanui deposits (Online Supplementary Table 2) and Huckleberry Ridge (Myers et al. 2016) are high-silica rhyolite in composition (SiO_2 = 75-77 wt%, volatile-free). For the 38 REs analyzed for H_2O and CO_2, lengths ranged from 100-450 µm, providing 4-17 analyzed spots per RE to define profiles (Fig. 2, Table 2). The RE lengths differed by deposit (Supplementary Fig. 2), with the Bishop (100-400, median 240 µm) and Oruanui (140-450, median 255) containing larger and more variable length REs compared to the Huckleberry Ridge (110-230 µm, median 170 µm). Interior volatile concentrations (H_2O, CO_2) of the REs are as follows: Bishop H_2O = 3.0-5.4 wt%, CO_2 = 53-240 ppm; Oruanui H_2O = 1.9-4.0 wt%, CO_2 = 25-100 ppm; and Huckleberry Ridge H_2O = 2.0-3.4 wt%, CO_2 = 50-450 ppm (Fig. 3). The H_2O and CO_2 profiles from REs (n = 9) in the Huckleberry Ridge initial fall deposits were previously published and discussed (Myers et al. 2016). In this paper, we present refined ascent rates for these REs using the modified decompression code presented below so the results can be directly compared with values inferred for the Bishop and Oruanui samples.

Many REs from Bishop and Oruanui have interior H_2O and CO_2 concentrations that are lower than enclosed MIs in quartz from the same deposits, though there is some overlap (Fig. 3). In contrast, for Huckleberry Ridge, there is complete overlap between RE interior and MI values. However, this is largely a reflection of the unusually wide range of MI H_2O values for Huckleberry Ridge (Myers et al. 2016), in contrast to Bishop and Oruanui, which show much narrower ranges of values for H_2O in MIs. Although enclosed MIs acquire a certain H_2O and CO_2 concentration at the time of trapping, their H_2O concentration can be modified by post-entrapment diffusion of H through the host quartz (Qin et al. 1992; Severs et al. 2007). This can occur during long-term storage and/or slow ascent towards the surface (e.g. Myers et al. 2016). Following Myers et al. (2016), we interpret MIs with lower H_2O concentrations at a given CO_2 content to have been affected by diffusive loss during slow ascent, and we assume that the highest H_2O values reflect the H_2O of the melt inclusion after prolonged magma storage at high temperature. Of the three eruptions studied, the Bishop MIs show the least effects of diffusive H_2O loss during ascent (i.e., the least variation in H_2O for a given CO_2 content), Huckleberry Ridge shows the most, and Oruanui is intermediate (see Fig. 3). Interestingly, only the Bishop fall deposits have interior RE concentrations that extend back to values for the MI H_2O concentrations that likely reflect the storage conditions for MIs before ascent began (Fig. 3).

All measured profiles presented here preserve gradients of H_2O and CO_2 (when present) towards their mouths, with longer REs occasionally showing more variability in their interiors (Supplementary Table 1, Supplementary Fig. 3). There were three REs sampled from the upper portions of the Huckleberry Ridge (sample MM3, n = 1) and Bishop (sample BTMMF9-1, n = 2) fall deposits that have much flatter profiles of H_2O vs. distance, and preserve very low H_2O concentrations (1-1.5 wt.%). These REs were sampled from fall deposit layers directly beneath thick ignimbrite (Table 1). We interpret these flatter profiles to be the result of post-depositional heating of the fall deposit by ignimbrite (e.g. Wallace et al. 2003), which allowed for continued H_2O diffusion to occur after emplacement (Supplementary Fig. 4). Additionally, there are four profiles (2 from Bishop, 2 from Oruanui) that, although they preserve gradients, have interior concentrations corresponding to pressures below 30 MPa (H_2O concentrations between 1.8-2.1 wt.%, no CO_2), suggesting prolonged reequilibration in the conduit at low pressures that approach the depth of fragmentation. The ascent rates calculated from these seven REs are not shown in any of the figures, but their profiles can be found in Supplementary Table 1.

Thirteen of the remaining 31 REs preserve no measureable CO_2. These are all from the early Bishop and Oruanui deposits, in which CO_2 concentrations in co-erupted, fully enclosed MIs are relatively low (maximum CO_2: early Bishop F1-F8 120 ppm, Oruanui 200 ppm, Fig. 3) compared to those of the Huckleberry Ridge (maximum CO_2 800 ppm: Fig. 3). Three REs from the Bishop fall deposit (F9), sampled in a location where no overlying ignimbrite was deposited, have normal H_2O profiles and contain CO_2 contents between 220-280 ppm, higher than all MIs measured from the earlier parts of the fall deposit. These F9 CO_2 contents extend to slightly higher values than are found in F9 melt inclusions but overlap with the high end of the range for coeval Ig2Ea ignimbrite and the low end of the range for late-erupted Bishop Tuff (Wallace et al. 1999; Roberge et al. 2013).

Modeling of diffusive losses of H_2O and CO_2 from reentrants

We used a 1-D forward diffusion numerical model modified from Liu et al. (2007) for fitting the measured H_2O and CO_2 profiles in each RE. In the Liu et al. model, H_2O and CO_2 diffuse through a melt-filled reentrant in response to changing external boundary conditions governed by magma decompression. The boundary condition at the contact between the host melt and the rim of the RE is based on the melt H_2O and CO_2 solubility at a given pressure, updated at each decompression step, and assumed to be in equilibrium with the gas bubbles present in the melt outside the crystal (Liu et al. 2007). Equilibrium concentrations are dependent on temperature, pressure, and gas phase composition (Liu et al. 2005). If this assumption were to be relaxed, the dissolved H_2O and CO_2 at the RE rim would likely be more elevated, by an amount that would depend on the degree of vapor-melt disequilibrium. One requirement to ensure that near-equilibrium exchange of volatiles between the rim of the RE and external melt can potentially be maintained is visual confirmation of a bubble wall at the mouth of each RE (Lloyd et al. 2014). Although bubbles were noted at the mouths of Bishop and Oruanui REs (Supplementary Fig. 1), they are less frequently observed in the Huckleberry Ridge REs. However, Myers et al. (2016) showed that using the glass adhering to the quartz rim as the exterior boundary position provided an adequate fit to measured profiles. Diffusion is assumed to be negligible once the sample has reached the fragmentation level, because the timescale between fragmentation and quenching of pyroclasts in the plume is likely to be very short (Liu et al. 2007; Humphreys et al. 2008). Estimates of fragmentation pressure for hydrous rhyolitic magmas are in the range of 10-30 MPa based on the vesicularities of pumice clasts and H_2O contents preserved in matrix glasses (Thomas et al. 1994; Gardner et al. 1996) as well as critical bubble volume fraction (Sparks 1978). Although fragmentation pressure may fluctuate during the course of an eruption (Melnik and Sparks 2002; Dufek and Bergantz 2005), we chose a constant value of 10 MPa and later evaluate how alternative values would affect the inferred ascent rates.

We created a Matlab version (a copy of the code can be requested from M. Myers) of the 1-D decompression model of Liu et al. (2007), and updated the diffusivity of CO_2 in rhyolitic melt as a function of temperature, pressure and water content using Zhang et al. (2007). The updated CO_2 diffusivities result in decompression rates that are up to 1.2x faster than those calculated by Liu et al. (2007) (see Supplementary Fig. 5 and Supplementary Table 3). By comparing our measured H_2O and CO_2 profiles to simulated profiles for various decompression rates and amounts of initial exsolved gas, both considered free parameters in all model runs, we can constrain the ascent conditions that most closely reproduce our FTIR-measured profiles. Because CO_2 diffuses at a slower rate than H_2O, modeling both gradients simultaneously provides more robust constraints on ascent timescales. However, as previously noted, 13 out of the 31 REs measured (all from Bishop and Oruanui deposits) have no measureable CO_2, and were thus modeled based solely on their H_2O profiles. The significance of the absence of CO_2 is discussed further in the discussion section.

Starting pressures determined from volatile solubility relationships are constrained either from co-genetic (i.e. same eruptive layer) melt inclusion H_2O and CO_2 measurements (Myers 2017) or the volatile concentrations in the innermost part of the RE analyzed (Supplementary Table 1). The RE profiles tend to plateau in the RE interior, suggesting that the plateau values represent the starting H_2O and CO_2 conditions at the time of final ascent. However, to further evaluate the results from both starting conditions (MI vs. RE interior), we model both scenarios.

All models were run assuming constant decompression rate and isothermal conditions, with temperature estimates as follows: Bishop 740 ºC, Oruanui 780 ºC, and Huckleberry Ridge 800 ºC (see Supplementary Material for discussion). Although the assumption of isothermal ascent is most probably met by an explosive, plinian eruption (Mastin and Ghiorso 2001), we consider how calculated ascent rates would shift for each system if the magma temperature were 20 ºC cooler (to evaluate the effect of cooling on calculated ascent rates).

To objectively choose the best-fit profile, we added an iterative grid-search function to optimize fitting of the measured profiles. This function allows the user to define a range of plausible decompression rates (MPa/s) and initial exsolved gas concentrations, which the model cycles through. After each ascent simulation with one set of input parameters, the chi-squared error representing the goodness-of-fit between the modeled profile points and the measured concentrations is calculated according to:

$$\chi^2=[((H_2O_{mod}-H_2O_{meas})/error_{H2O})^2+((CO_{2mod}-CO_{2meas})/error_{CO2})^2]/n, \qquad \text{Eq. 3}$$

where H_2O and CO_2 species are weighted according to their analytical uncertainties and *n* is the number of measured data points. A similar method was employed by Ferguson et al. (2016) for their analysis of fits to olivine-hosted basaltic REs from Kilauea volcano, Hawaii. For all model runs presented in this paper, we used a standard deviation error for H_2O of ±0.2 or 0.3 wt% and for CO_2, ±20 or 30 ppm (specified in Table 3). After all simulations have been run, the decompression rate and initial exsolved gas fraction that produce the lowest misfit (χ^2) are taken to yield the best-fit profile. Although in most model runs a range of decompression rates yields χ^2 values that indicate acceptable fits (see d*P*/d*t* error bar values in Table 2), profiles from these decompression rates produce slopes that are visually poorer fits to the data than those produced by the best-fit decompression rate (Fig. 4). This is because the range of decompression rates that fit the data is strongly controlled by the analytical uncertainties of the H_2O and CO_2 measurements.

Best-fit ascent rates

Using the H_2O and CO_2 concentrations of MIs from each sample as starting conditions requires decompression rates between 0.0002-.03 MPa/s to reproduce measured RE profiles (Table 3). However, using MIs to define the starting conditions generally yields poorer fits to the data, with only 7 RE profiles generating χ^2<1, and 4 of these yielding comparable fits (within 0.1 χ^2) to those produced using the RE interior H_2O and CO_2 as starting conditions. The implications of this result will be discussed later. Given these poor fits, we focus on the best-fit decompression rates that use the RE interiors as starting conditions. Using the H_2O and CO_2 concentrations in the interiors of the REs as starting conditions, best-fit decompression rates for the 31 REs modeled range from 0.003-0.5 MPa/s, with χ^2≤1 for all 31 profiles. These decompression rates were converted into ascent rates using the difference between the starting pressure, based on H_2O and CO_2 solubility relationships, and the fragmentation pressure, which was assumed to be 10 MPa. Starting pressures were converted to depth using a mean crustal density of 2600 kg/m^3, assuming lithostatic conditions. Using the same conversion, a fragmentation pressure of 10 MPa translates to ~400 m depth. However, using a lithostatic assumption for converting pressure to depth is likely not valid for estimating the fragmentation depth (Mastin 2005; Gonnermann and Manga 2013). Based on numerical conduit models, the depth of fragmentation ranges between 1 and 2.5 km (Mastin 2005; Gonnermann and Manga 2013, Melnik et al. 2005). Here we adopt the fragmentation depth to be 1 km. It should be noted that the effect of using 1500 m verses 500 m decreases the distance over which diffusion can occur, which serves to slow calculated ascent rates by a factor of 1.7-2.0x.

Best-fit profiles for all REs yield ascent rates between 0.06-13 m/s, spanning roughly two orders of magnitude (Fig. 5). These values overlap with inferred ascent rates reported in the literature for explosive eruptions across a range of eruptive volumes and magma compositions (Rutherford 2008), but are on the slower end of values based on analytical and numerical modeling for plinian rhyolitic eruptions (5-30 m/s; see reviews by Rutherford 2008; Gonnermann and Manga 2013). The majority (75%) of ascent rates presented here are between 0.4 and 5 m/s. These ascent rates yield magma ascent times as short as tens of minutes to as long as 2.5 hours. The fastest ascent rates are found in the upper parts of the Bishop fall deposit, coming from as deep as 7.0 km (160 MPa), whereas the slowest ascent rates (0.06-0.48 m/s) are from the earliest phases of the Oruanui eruption (Fig. 5). Notably, these slowest ascent rates are associated with the initial two phases of the Oruanui eruption, but ascent rates are uniformly higher for phase three of the eruption, indicating that average ascent rates increase upwards through the stratigraphy (Fig. 5). The Oruanui phase 3 REs are also strongly correlated with higher RE interior pressures and higher RE rim equilibration pressures (R^2=0.84; Fig. 6). This observation, however, could change with additional measurements (currently n = 3 for Phase 3 REs). For the Bishop and Huckleberry Ridge eruptions there is no strong up-section variation in ascent rate (Fig. 5). For all three eruptions, especially Bishop, the later erupted REs preserve higher interior pressures (Fig. 6; Supplementary Fig. 6).

DISCUSSION

Ascent rates and eruption characteristics

There is a large overlap in the ascent rates observed in the initial fall deposits from all three systems (Fig. 5). This suggests that although the eruptions had differences in initial behavior inferred from field evidence (start/stop vs. continuous activity), the differences do not correspond to obvious systematic differences in the final ascent rates recorded by REs. However, as noted above, the fastest ascent rates are recorded in several fall layers from the Bishop Tuff, an eruption that has little evidence for time gaps in deposition. By contrast, the slowest are found in the first two phases of the Oruanui eruption, which had relatively weak eruption styles, were separated by a time break of weeks to months, and have been linked to control by an external rifting event (Wilson 2001; Allan et al. 2012). The third phase of the Oruanui eruption, however, lacks the very slow ascent rates that are observed in the first two phases. The transition from phase two to phase three was associated with a shift from a focused vent area on the northeastern margin of what became the structural caldera to an elongate vent alignment on its eastern edge (Wilson 2001). The association of faster ascent rates with an inferred escalation in eruption intensity and more extensive vent configuration suggests that final ascent rates may be related to vent geometry and mass flux. However, there is no notable up-section increase in ascent rates observed in the Bishop Tuff, including at the onset of Glass-Mountain-derived obsidian lithics (in upper F8, Fig. 5), which is taken as evidence for caldera ring fracture development. One possibility could be that during this period of the Bishop eruption, fall and flow activity may have been from separate and evolving conduits (Wilson and Hildreth 1997), which would obscure a record of any relationships between ascent rate and changes in conduit and vent configuration.

Further investigation of the connection between ascent rate, mass flux and vent geometry would require application to a system with a simple vent geometry and well constrained variations in mass discharge rate.

A key result from the RE data is that the melt at the mouths of REs preserves a record of greater apparent quenching depths for REs that experienced higher ascent rates. This is most robust for the Oruanui eruption ($R^2 = 0.84$: Fig. 6) and suggests one or both of the following: (1) our assumption of a constant fragmentation pressure (10 MPa) is incorrect, and instead, the fragmentation level became deeper as the eruptions progressed, or (2) for REs that experienced greater ascent rates, there was a greater extent of disequilibrium at the boundary between the external melt and the melt in the mouth of the RE.

Evaluation of Assumptions

The error bars on modeled ascent rates presented in Figs. 5, 6 and 7 represent the range of decompression rates that produce acceptable fits to the measured data ($\chi^2 <1$), taking into account analytical uncertainties. However, as previously mentioned, there are several factors and assumptions that influence the deduced ascent rates, including: (1) depth of fragmentation (D_f), (2) final pressure of fragmentation (P_f), (3) isothermal ascent (T), (4) starting pressure (P_i), (5) assumption of constant decompression rate, and (6) assumption of vapor-melt equilibrium at the RE mouth. Assumptions (5) and (6) are simplifications we adopted to reduce the number of free parameters. At this stage, we do not attempt to quantify how a more complex model would compare to the simplified model results. Fig. 7 summarizes how varying parameters (1)-(4) individually for Bishop Tuff REs affects the final ascent rates compared to our preferred model where D_f = 1000 m, P_f = 10 MPa, T = magmatic temperature, and P_i = pressure calculated for reentrant interior values of dissolved H_2O and CO_2. A decrease in temperature of 20°C, such as might occur from cooling in the conduit, or a change in the fragmentation depth (500 m or 1500 m instead of 1000 m) have relatively smalls effect on calculated ascent rates, shifting values by a factor of 1.2-2.5x. Using the mouth saturation pressure for the pressure of fragmentation slows ascent rates by a factor of 1.1-3x. Similarly, using the melt inclusions H_2O and CO_2 as starting conditions decreases ascent rates by a factor of 1.1-3.5x. However, it should be noted that our preferred model generally produces better model fits for the measured profiles, especially compared to using MI concentrations as starting conditions. Most importantly, the extent of these variations only serves to shift our reported ascent rates (Fig. 7), but does not reduce the 2 orders-of-magnitude range that is reflected in the 31 measured H_2O and CO_2 diffusion profiles.

Evidence for a two-stage decompression history

One notable observation from our dataset is the significant offset between the starting pressures derived from the innermost H_2O and CO_2 concentrations in the REs and the higher pressures associated with the pre-eruptive storage depth of co-erupted MIs (Figs. 3, 6). We found that the best fits to the RE volatile concentration profiles were achieved when using the innermost RE concentrations, which tend to plateau to constant values, as the starting condition (Supplementary Fig. 3). In contrast, when the initial H_2O and CO_2 concentrations of MIs were used as starting conditions, the chi-squared misfits were found to be 1.2-15x worse for all but four REs (Table 3). Although ascent rates that use MI values as starting conditions are consistently slower than those calculated using the RE interior concentrations, and provide poorer fits, all estimates fall within a factor of 6 (Fig. 7; Supplementary Fig. 7).

For the 27 REs where the interior RE concentrations provide better starting conditions for the measured profiles (i.e. produce model profiles that are better fits to the measured data points), a mechanism is then required to explain the shallower starting depths, and associated H_2O and CO_2 concentrations, compared to the values for MIs. We interpret this offset to suggest that there was a deeper, and initially slower, decompression period experienced by the REs, which allowed them to partially or fully re-equilibrate with the external melt prior to final, more rapid ascent (Fig. 8). A similar explanation was called upon to explain the wide H_2O variations measured in MIs within individual fall horizons of the Huckleberry Ridge initial fall deposits (Myers et al. 2016). In Myers et al. (2016), the range of H_2O variations was interpreted to represent variable loss of H by diffusion through the quartz host during slow decompression or shallow storage that led to degassed melt surrounding the quartz. We interpret the offset recorded by values for interior RE plateaus with respect to the co-erupted MIs (the highest values of which represent storage conditions) to result from partial reequilibration as the magma initially fed from the storage region into the conduit system. In this interpretation, the measured RE volatile gradients near the outlets of REs are recorders of the faster, final ascent rate, but do not represent the entire ascent history of a given host crystal (Fig. 8). Note that a two-stage decompression model was similarly required to model the H_2O, CO_2 and S profiles of four mafic REs in olivine from the October 17th, 1974, eruption of Volcan de Fuego, Guatemala (Lloyd et al. 2014). Although good fits could be achieved for their H_2O and S profiles using a constant decompression model starting from the MI storage region, to also accurately model the CO_2 profiles, an initial slower decompression period between MI storage and a shallower depth was found to be necessary.

Timescales of Initial Decompression

We can estimate the timescale of initial, slower decompression by modeling the time required for the melt in an RE to re-equilibrate from starting H_2O and CO_2 concentrations that are similar to those in the MIs to final values that match the innermost part of each RE (Fig. 8, Table 2). Two approaches were used. In the first, we adopted an instantaneous decompression step followed by a re-equilibration period at constant pressure. In this scenario, the RE starts with uniform H_2O and CO_2 concentrations that are the same as in co-erupted MIs. The exterior boundary condition, following the instantaneous decompression, is fixed to the H_2O and CO_2 concentrations measured in the interior of each individual RE. We consider the RE to have re-equilibrated with the external melt when flat plateaus have developed in the RE interior and where profiles have concentrations of H_2O within 0.1 wt% and CO_2 within 10 ppm of re-equilibration values (i.e., well within the measurement error). This method provides a minimum estimate for the times required for RE re-equilibration, which are <1 to 13 hours (Bishop), 4 hours to 3 days (Oruanui), and 1.5 to 30 hours (Huckleberry Ridge: Figs. 9, 10).

The second approach is to assume constant slow decompression along a degassing path from the pre-eruptive storage region to the same shallower depth, above which the decompression rate rapidly increases, producing the modeled reentrant gradient. To model this situation, we applied our constant decompression model to all REs, and used the same starting and ending H_2O and CO_2 conditions and criteria for when reequilibration has been achieved as described above. For Bishop REs, the initial slower decompression rates range from $5.0 \times 10^{-3} – 4.5 \times 10^{-4}$ MPa/s, implying 3 hours to 4.5 days of slower ascent (Fig. 10). For Oruanui, the slower decompression rates ($1.0 \times 10^{-3} – 2 \times 10^{-4}$ MPa/s) require reequilibration times as long as 1-7 days. Lastly, the Huckleberry Ridge REs require decompression rates of $5.0 \times 10^{-3} – 2 \times 10^{-3}$ MPa/s, equating to times of 5 hours to 1 day, similar to the range preserved using the step function. However, these continuous decompression timescales for the Huckleberry REs could only be calculated for 5 of 9 REs. For the remaining 4 REs, no plausible degassing path could be found between their 'starting MI' state and their preserved RE interior H_2O and CO_2 conditions (Fig. 3). This could be due to significant reorganization of the eruptible melt bodies surrounding the quartz host prior to eruption (see discussion in Myers et al. 2016), meaning that an accurate estimate for their starting melt composition cannot be well constrained. The Bishop and Oruanui REs that require the longest reequilibration time tend to have H_2O and CO_2 concentrations in their interiors that record the shallowest depths and, at least in the Bishop fall deposit, generally lack CO_2 (Figs. 3, 7). This last observation confirms the requirement for an initially sluggish stage of magma ascent, because CO_2 takes longer to re-equilibrate than H_2O.

For the Bishop Tuff, the H_2O and CO_2 concentrations measured in the interiors of REs, appear to trend towards deeper pressures in samples from higher in the stratigraphy (Figs. 3, 6). One RE interior concentration from the upper fall layer (F9) even overlaps with the starting MI range (Fig. 6). Interestingly, by this point in the Bishop eruption roughly 2/3 of the total erupted volume had been evacuated. We do not have RE data for such late stages of the Huckleberry Ridge and Oruanui eruptions, as the samples analyzed here represent only the first 1-2 % of the total volume erupted. We infer this observation for the Bishop Tuff to represent the transition between where there is the need for a two-stage model to reproduce the RE profiles, to the situation where modeling of the measured profiles can accurately use the MI starting conditions. This changeover is reflected in the diminishing χ^2 (misfit) from using RE interior volatile concentrations when compared to using the volatile concentrations of co-erupted MIs as starting conditions for F9 REs (Table 3). These changes suggest a maturing of the conduit system, where the initial slow period of magma ascent results from a less developed or less well integrated conduit system, which evolves over the course of the eruption such that later erupted magma experiences little to no initial slow decompression. This hypothesis is consistent with the qualitative model of Scandone et al. (2007), who argued that there is a development phase leading up to a large explosive eruption during which the storage region and the conduit system become increasingly interconnected. In the Bishop case, our results show that maturing of the conduit system occurred in parallel with the development of multiple vents.

Comparison of MI and RE Reequilibration Times

The scatter in measured H_2O concentrations for fully enclosed MIs in the Huckleberry Ridge Tuff (~1.0-4.5 wt.%) has been interpreted to reflect diffusive losses of H through the quartz lattice during slow ascent and shallow storage on a timescale of days just prior to eruption (Myers et al. 2016). Because diffusive loss of H from MIs occurs on similar timescales as those we have deduced for the initial slow decompression stage experienced by the REs (days), a detailed comparison of the timescales from REs and MIs provides a test of our interpretation regarding initial slow decompression in the three magmatic systems.

Determining the timescale for diffusive loss of H from an MI requires information about the following parameters: (1) estimates for initial MI H_2O values at the time of trapping or following extended storage time at high temperature, (2) estimates of external H_2O concentrations at some lower pressure at which the MI has partially or fully reequilibrated, (3) magmatic temperature, and (4) the size of each inclusion and distance to rim (see Supplementary Material, Myers et al., 2016 and Myers 2017 for details on methods and assumptions used). To determine the initial H_2O concentration for each MI we assumed that H_2O behaved moderately incompatibly through partial loss to a vapor phase during vapor-saturated crystallization (see Myers et al. 2016 for Huckleberry Ridge, and Myers 2017 for Bishop and Oruanui reconstructions). For (2), we assumed that the MIs partially reequilibrated in external melts that had H_2O concentrations similar to the plateau values of H_2O found in the interiors of REs from the same sample. For the Huckleberry Ridge Tuff, 66% (total n = 94) of MIs require residence of >1 day in a partially degassed melt to reproduce their measured H_2O concentrations, with 42 inclusions requiring 1-5 days, and the lowest measured H_2O values (n = 20) requiring up to ~10 days (Fig. 10). Applying the same model to reproduce the H_2O ranges (~4.0-6.0 wt.%) measured from the first two fall layers of the Bishop Tuff, 65% of inclusions (n = 45) experienced no observable diffusive loss, equating to <24 hours residence in partially degassed melt in the conduit system (Myers 2017). Of the 16 Bishop MIs that show evidence for diffusive losses, 4 require 1-5 days of lower pressure diffusive loss, and 12 spent >5 days in the conduit system. Lastly, the first and third fall layers of the Oruanui display a wide range of H_2O contents (~3.0-5.8 wt%) in MIs for restricted ranges in CO_2, similar to the scatter observed in the Huckleberry Ridge (Fig. 3). Of the 46 inclusions (45%) that experienced >1 day in the conduit, 35 require 1 to 5 days of diffusive loss to a degassed melt, and 11 require >5 days (Myers 2017).

There is considerable overlap in the timescales of diffusive loss recorded by MIs and REs, but for all three eruptions the timescales of diffusive loss for MIs extend to longer times than are calculated for the initial slow decompression stage experiences by the REs (Fig. 10). The general agreement between the different approaches provides strong evidence for an early, slower phase of decompression during the opening stages of these eruptions, which we interpret to result from the lack of fully mature, interconnected pathways from the region of magma storage to the lower parts of the conduit system early in the eruptions. For all three systems, this slow decompression phase occurred over timescales of hours to days, prior to the final, rapid ascent (<1-3 hours) that fed the explosive eruptions (Fig. 10). The extension of the MI values towards longer times than are seen for the REs could have several possible explanations. First, the diffusivity of H in quartz is poorly constrained, and the temperature dependence of the diffusivity is even less well known (see Myers et al., 2016). Second, for Huckleberry Ridge, the initial H_2O and CO_2 conditions for the MIs are less well constrained than for Oruanui and Bishop, because trace element chemistry suggests significant reorganization of multiple magma bodies between the time of MI entrapment and the time of final storage prior to eruption (Myers et al. 2016). Third, REs that experienced a longer slow decompression stage may exist but were not chosen for analysis.

IMPLICATIONS

The dataset presented here represent results of the first study to determine ascent rates using concentration profiles for H_2O and CO_2 in quartz-hosted reentrants in rhyolitic magmas, with the aim of constraining the timescales of the early stages of activity for three contrasting explosive eruptions. Our results and comparison with decompression rates estimated from diffusive loss of H from MIs, demonstrate the potential of modeling gradients in reentrants to estimate ascent rates and timescales from erupted volcanic products. The majority of reentrants (75% of n = 31) require ascent rates between 0.4 and 5 m/s, equating to ascent times in the conduit of tens of minutes up to a few hours. Re-equilibration of the interiors of REs to lower H_2O and CO_2 conditions when compared to their co-erupted MIs suggests, however, that the majority of REs experienced an initially slower ascent period, on the order of several hours to several days, prior to final ascent and quenching. This inference is supported by the scatter in measured H_2O concentrations from enclosed MIs, also interpreted to reflect slow initial decompression accompanying ascent from the magma reservoir (Myers et al. 2016; Myers 2017). Ascent times estimated solely by using the measured volatile gradients preserved in the REs are thus minimum values in these systems, and can miss hours to days of slower initial ascent conditions.

By collecting samples from stratigraphically controlled levels in the deposits we are able to compare our modeled ascent rates with field interpretations of the progress of each eruption, in order to provide context for our results. We observe that in the Oruanui samples there is a noted increase in the ascent rates for layers deposited during periods of increased eruptive flux (Phase 3). The faster ascent rates are also correlated with greater inferred pressures in the interiors and mouths of the REs. The slowest ascent rates determined in this study come from the first two Oruanui eruption phases, which were interpreted to have been mobilized by an external rifting event (Wilson 2001; Allan et al. 2012), and as such, may have involved magma that was not strongly overpressured. The fastest rates modeled in this study (8-13 m/s) are from the Bishop Tuff, the only system for which our sample set covers much of the eruption duration and the only of the three eruptions that shows no field evidence for long time gaps in deposition (Fig. 5). Additionally, late-erupted Bishop REs (fall layers 8 and 9, close to the time of caldera-formation) have interior H_2O and CO_2 concentrations that approach pre-eruption magmatic values. We interpret the temporal decrease in the timescale of the initial slow decompression in the Bishop eruption to represent the maturing and increasing interconnectivity of the conduit system. Ascent rates derived from modeling of reentrants thus provide key insights into the behavior of magma in the hours to days before it reaches the surface. Linkages between RE and MI timescales and field evidence offer promise in understanding the dynamic processes involved in the initiation of voluminous eruptions, as well as providing first-order estimates of the timescales of unrest that might be used for improving warning of impending activity.

ACKNOWLEDGEMENTS

We thank Christy Hendrix and Stacey Gunther in the Yellowstone Research Office for permission (YELL-05248) to work in Yellowstone National Park. Financial support was provided by National Science Foundation grant EAR-1524824 to PW. The presentation of this manuscript was greatly improved with the constructive and thorough reviews by J. Hammer, H. Gonnermann and an anonymous reviewer.

REFERENCES CITED

Allan, A.S.R., Wilson, C.J.N., Millet, M.-A., and Wysoczanski, R.J. (2012) The invisible hand: tectonic triggering and modulation of a rhyolitic supereruption. Geology, 40, 563-566.

Baker, D.R., Lang, P., Robert, G., Bergevin, J.-F., Allard, E., and Bai, L. (2006) Bubble growth in slightly supersaturated albite melt at constant pressure. Geochimica et Cosmochimica Acta, 70, 1821–1838.

Behrens, H., Tamic, N., and Holtz, F. (2004) Determination of the molar absorption coefficient for the infrared absorption band of CO_2 in rhyolitic glasses. American Mineralogist, 89, 301-306.

Cashman, K.V. (2004) Volatile controls on magma ascent and eruption. In R.S.J. Sparks and C.J. Hawkesworth, Eds., The State of the Planet: Frontiers and Challenges in Geophysics. American Geophysical Union Geophysical Monographs, 150, p. 109-124.

Castro, J.M., and Gardner, J.E. (2008) Did magma ascent rate control the explosive-effusive transition at the Inyo volcanic chain, California? Geology, 36, 279-282.

Christiansen, R.L. (2001) The Quaternary and Pliocene Yellowstone Plateau volcanic field of Wyoming, Idaho, and Montana. U.S. Geological Survey Professional Papers, 729-G, p. 1-143.

Dingwell, D.B. (1996) Volcanic dilemma: flow or blow? Science, 273, 1054.

Donovan, J.J., Kremser, D., Fournelle, J.H., 2007. Probe for Windows User's Guide and Reference, Enterprise Edition. Probe Software, Inc., Eugene, OR.

Dufek, J., and Bergantz, G.W. (2005) Transient two-dimensional dynamics in the upper conduit of a rhyolitic eruption: A comparison of closure models for the granular stress. Journal of Volcanology and Geothermal Research, 143, 113-131.

Eichelberger, J.C., Carrigan, C.R., Westrich, H.R., and Price, R.H. (1986) Non-explosive silicic volcanism. Nature, 313, 598-602.

Ferguson, D.J., Gonnermann, H.M., Ruprecht, P., Plank, T., Hauri, E.H., Houghton, B.F., and Swanson, D.A. (2016) Magma decompression rates during explosive eruptions of Kīlauea volcano, Hawaii, recorded by melt embayments. Bulletin of Volcanology, 78, 71.

Gardner, J.E. (2007) Heterogeneous bubble nucleation in highly viscous silicate melts during instantaneous decompression from high pressure. Chemical Geology, 236, 1-12.

Gardner, J.E., Thomas, R.M.E, Jaupart, C., and Tait, S. (1996) Fragmentation of magma during Plinian volcanic eruptions. Bulletin of Volcanology, 58, 144-162.

Gonnermann, H.M., and Manga, M. (2013) Dynamics of magma ascent in the volcanic conduit. In S.A. Fagents, T.K.P. Gregg and R.M.C. Lopes, Eds., Modeling Volcanic Processes: The Physics and Mathematics of Volcanism, p. 55-84. Cambridge University Press, Cambridge, U.K.

Hildreth, W., and Mahood, G.A. (1986) Ring-fracture eruption of the Bishop Tuff. Geological Society of America Bulletin, 97, 396-403.

Hildreth, W., and Wilson, C.J.N. (2007) Compositional zoning of the Bishop Tuff. Journal of Petrology, 48, 951-999.

Humphreys, M., Menand, T., Blundy, J.D., and Klimm, K. (2008) Magma ascent rates in explosive eruptions: constraints from H_2O diffusion in melt inclusions. Earth and Planetary Science Letters, 270, 25-40.

Leschik, M., Heide, G., Frischat, G.H., Behrens, H., Wiedenbeck, M., Wagner, N., Heide, K., Geißler, H., and Reinholz, U. (2004) Determination of H_2O and D_2O contents in rhyolitic glasses. Physics and Chemistry of Glasses, 45, 238-251.

Liu, Y., Zhang, Y., and Behrens, H. (2005) Solubility of H_2O in rhyolitic melts at low pressures and a new empirical model for mixed H_2O–CO_2 solubility in rhyolitic melts. Journal of Volcanology and Geothermal Research, 143, 219-235.

Liu, Y., Anderson, A.T., and Wilson, C.J.N. (2007) Melt pockets in phenocrysts and decompression rates of silicic magmas before fragmentation. Journal of Geophysical Research, 112, B06204.

Lloyd, A.S., Ruprecht, P., Hauri, E.H., Rose, W., Gonnermann, H.M., and Plank, T. (2014) NanoSIMS results from olivine-hosted melt embayments: magma ascent rate during explosive basaltic eruptions. Journal of Volcanology and Geothermal Research, 283, 1-18.

Mangan, M., and Sisson, T. (2000) Delayed, disequilibrium degassing in rhyolite magma: decompression experiments and implications for explosive volcanism. Earth and Planetary Science Letters, 183, 441-455.

Mastin, L.G. (2002) Insights into volcanic conduit flow from an open-source numerical model. Geochemistry, Geophysics, Geosystems, 3, doi:10.1029/2001GC000192.

Mastin, L.G. (2005) The controlling effect of viscous dissipation on magma flow in silicic conduits. Journal of Volcanology and Geothermal Research, 143, 17-28.

Mastin, L. G., and Ghiorso, M. S. (2001) Adiabatic temperature changes of magma-gas mixtures during ascent and eruption. Contributions to Mineralogy and Petrology, 141, 307-321.

Melnik, O., and Sparks, R.S.J. (2002) Modelling of conduit flow dynamics during explosive activity at Soufrière Hills Volcano, Montserrat. In T.H. Druitt and B.P. Kokelaar, Eds., The Eruption of Soufriere Hills Volcano. Montserrat, from 1995 to 1999. Geological Society of London Memoirs, 21, p. 307-317.

Melnik, O., Barmin, A.A., and Sparks, R.S.J. (2005) Dynamics of magma flow inside volcanic conduits with bubble overpressure buildup and gas loss through permeable magma. Journal of Volcanology and Geothermal Research, 143, 53-68.

Myers, M.L. (2017) Storage, ascent, and release of silicic magma in caldera-forming eruptions, 216 p. PhD. thesis, University of Oregon, Eugene.

Myers, M.L., Wallace, P.J., Wilson, C.J.N, Morter, B.J., and Swallow, E.J. (2016) Prolonged ascent and episodic venting of discrete magma batches at the onset of the Huckleberry Ridge supereruption, Yellowstone. Earth and Planetary Science Letters, 451, 285-297.

Newman, S., and Lowenstern, J.B. (2002) VolatileCalc: a silicate melt–H_2O–CO_2 solution model written in Visual Basic for Excel. Computers and Geosciences, 28, 597-604.

Qin, Z., Lu, F., and Anderson, A.T. (1992) Diffusive reequilibration of melt and fluid inclusions. American Mineralogist, 77, 565-576.

Papale, P., Neri, A., and Macedonio, G. (1998) The role of magma composition and water content in explosive eruptions. 1. Conduit ascent dynamics. Journal of Volcanology and Geothermal Research 87, 75-93.

Roberge, J., Wallace, P.J., and Kent, A.J.R. (2013) Magmatic processes in the Bishop Tuff rhyolitic magma based on trace elements in melt inclusions and pumice matrix glass. Contributions to Mineralogy and Petrology, 165, 237-257.

Rotella, M.D., Wilson, C.J.N., Barker, S.J., Cashman, K.V., Houghton, B.F., and Wright, I.C. (2014) Bubble development in explosive silicic eruptions: insights from pyroclast vesicularity textures from Raoul volcano (Kermadec arc). Bulletin of Volcanology, 76, 862.

Rutherford, M.J. (2008) Magma ascent rates. In K.D. Putirka and F.J. Tepley III, Eds., Minerals, Inclusions and Volcanic Processes, 69, p. 241-271. Reviews in Mineralogy and Geochemistry, Mineralogical Society of America, Chantilly, Virginia.

DOI: https://doi.org/10.2138/am-2018-6225

Scandone, R., Cashman, K.V., and Malone, S.D. (2007) Magma supply, magma ascent and the style of volcanic eruptions. Earth and Planetary Science Letters, 253, 513-529.

Severs, M.J., Azbej, T., Thomas, J.B., Mandeville, C.W., and Bodnar, R.J. (2007) Experimental determination of H_2O loss from melt inclusions during laboratory heating: evidence from Raman spectroscopy. Chemical Geology, 237, 358-371.

Skirius, C.M. (1990) Pre-eruptive H_2O and CO_2 content of plinian and ash-flow Bishop Tuff magma, 237 p. Ph.D. thesis, University of Chicago.

Sparks, R.S.J. (1978) The dynamics of bubble formation and growth in magmas: a review and analysis. Journal of Volcanology and Geothermal Research, 3, 1-37.

Thomas, N., Jaupart, C., and Vergniolle, S. (1994) On the vesicularity of pumice. Journal of Geophysical Research, 99, 15633-15644.

Toramaru, A. (2006) BND (bubble number density) decompression rate meter for explosive volcanic eruptions. Journal of Volcanology and Geothermal Research, 154, 303-316.

Wallace, P.J., Anderson, A.T., and Davis, A.M. (1999) Gradients in H_2O, CO_2, and exsolved gas in a large-volume silicic magma system: Interpreting the record preserved in melt inclusions from the Bishop Tuff. Journal of Geophysical Research, 104, 20097-20122.

Wallace, P.J., Dufek, J., Anderson, A.T., and Zhang, Y. (2003) Cooling rates of Plinian-fall and pyroclastic-flow deposits in the Bishop Tuff: inferences from water speciation in quartz-hosted glass inclusions. Bulletin of Volcanology, 65, 105-123.

Wilson, C.J.N. (2001) The 26.5 ka Oruanui eruption, New Zealand: an introduction and overview. Journal of Volcanology and Geothermal Research, 112, 133-174.

Wilson, C.J.N. (2009) Physical Volcanology of the Huckleberry Ridge Tuff. In AGU Fall Meeting Abstracts (#V23C-2085).

Wilson, C.J.N., and Hildreth, W. (1997) The Bishop Tuff: new insights from eruptive stratigraphy. Journal of Geology, 105, 407-439.

Wysoczanski, R., and Tani, K. (2006) Spectroscopic FTIR imaging of water species in silicic volcanic glasses and melt inclusions: an example from the Izu-Bonin arc. Journal of Volcanology and Geothermal Research, 156, 302-314.

Zhang, Y., Xu, Z., Zhu, M., and Wang, H. (2007) Silicate melt properties and volcanic eruptions. Reviews of Geophysics, 45, RG4004.

DOI: https://doi.org/10.2138/am-2018-6225

Figure captions

Fig. 1. Generalized caldera outlines for the three rhyolitic supereruptions investigated in this study: Bishop (modified from Wilson and Hildreth 1997), Oruanui (modified from Wilson 2001), and Huckleberry Ridge (Myers et al. 2016). Stars on each map represent a sampling location, where in some cases the same fall layer was collected in multiple locations (see Table 1 for more information).

Fig. 2. (a) A compositional map of H_2O concentration in a Bishop reentrant (open melt pocket), where white boxes (22 x 22 μm) represent the aperture size of the analyzed area. (b & c) Photomicrographs of representative quartz crystals from the Huckleberry Ridge initial fall deposits, where each crystal contains several large melt inclusions and one large reentrant that extends out to meet adhering matrix glass.

Fig. 3. H_2O vs. CO_2 concentrations for melt inclusions, shown as circles, and reentrants, shown as diamonds, from the Bishop (top panel), Oruanui (middle panel) and Huckleberry Ridge (bottom panel) samples. All melt inclusion data can be found in Myers (2017). Additional melt inclusion data to complement our F1 dataset is plotted for the Bishop Tuff fall layers F2-F9, shown as plus signs, from Roberge et al. (2013), and a peach-colored field representing Ig2Ea (mid-Bishop compositions: Wallace et al. 1999) was added to provide compositional context for the three high CO_2 REs from unit F9. Light gray lines are isobars (values of constant pressure), black solid lines are open-system degassing trends, and black dashed lines represent closed-system degassing with 3 wt.% exsolved vapor phase (Newman and Lowenstern 2002). Vapor composition isopleths (in mol% H_2O) are shown as bold gray lines. For the Huckleberry Ridge (bottom panel), colored regions represent distinct melt compositional clusters based on MI data, which are inferred to represent distinct bodies of magma (Myers et al. 2016) for associated reentrants (colored to match).

Fig. 4. (a) Chi-squared misfit plot for a range of decompression rates. All decompression rates in the shaded region, between 0.018-0.1 MPa/s produce profiles that fall within the statistically valid $\chi^2 < 1$ region. (b) The three profiles produced from the decompression rate associated with misfit points A, B and C shown in (a). Profile 'B' represents the best-fit profile for the H_2O measurements, although A and C also represent acceptable fits, based on analytical uncertainties.

DOI: https://doi.org/10.2138/am-2018-6225

Fig. 5. Ascent rates modeled for individual reentrants, shown as diamonds, positioned according to their relative stratigraphic level within each eruption. The bottom of each diagram represents the earliest erupted material. Diamonds containing an X represent reentrants that lacked measurable CO_2, meaning ascent rates were constrained by modeling H_2O only. Shaded fields represent estimated ascent rates for rhyolitic magma based on alterative models. The blue field represents the ascent rates associated with the time it takes for H_2O to diffuse into a bubble and maintain equilibrium, with estimates from experimental work between 0.7 and 5 m/s (e.g. Baker et al. 2006; Gardner 2007: see Rutherford 2008 for review). The yellow field is an analytical model for rhyolitic magma ascent, yielding ascent rate estimates of 5-8 m/s (Papale et al. 1998). The red region, with rhyolitic ascent rates estimated between 5-30 m/s, comes from conduit flow models (Mastin 2002, 2005).

Fig. 6. Ascent rate versus pressure and depth for individual reentrants (diamonds). Pressures (MPa) are based on H_2O vs. CO_2 solubility, shown as colored diamonds for interior measurements, and open diamonds for the mouth or rim of each reentrant. A color gradient unique to each eruption designates whether a reentrant is from early or late in the eruptive stratigraphy sampled, as derived from field information (Fig. 5). Storage (or starting) depths are inferred from co-erupted melt inclusion H_2O vs. CO_2 concentrations (Myers 2017). Trend lines are for the reentrant mouths from the suite of REs for each of the eruptions.

Fig. 7. Comparison between the ascent rates calculated for Bishop REs using the same diffusion model, but with different starting assumptions. The preferred model represents the starting conditions that are presented in Figs. 5 and 6 (see discussion for more information). Each set of ascent rates involve changing one assumption from the preferred model. The error bars represent the range of dP/dt conditions that also produce acceptable fits to the measured profile (χ^2 <1). For those reentrants that lack an error bar, this represents a $\chi^2 \geq 1$.

Fig. 8. Simplified visualization of the offset between melt inclusion starting conditions and those preserved by the flat plateau of the reentrant H2O concentration profile (shown as squares). Phase 1 represents the initial slower decompression that allows for a reentrant to reequilibrate to lower H2O concentrations than it starts with, based on melt

DOI: https://doi.org/10.2138/am-2018-6225

inclusion data from the same sample. Phase 2 involves the timescale associated with creating the concentration gradient that is recorded in the outer part of the reentrant.

Fig. 9. Time of final ascent (tens of minutes to a few hours) determined from the best-fit model that recreated the measured concentration gradient, plotted verses re-equilibration time during the initial slow stage of decompression. Reequilibration is the time it takes for the volatile concentrations in the interior part of the reentrant to reequilibrate from values similar to those found in melt inclusions, assuming an instantaneous pressure change (step-function). Summing these two times would equate to the minimum time estimate each RE spent within the conduit system.

Fig. 10. Relative probability density function (kernel distribution) for the timescale of the initial slow decompression phase estimated from: (top) H diffusion through quartz from enclosed melt inclusions to a changing external melt (n = 45 Bishop, n = 94 Huckleberry Ridge, n = 103 Oruanui; Myers et al. 2016; Myers 2017); (2) reentrant reequilibration assuming an instantaneous drop in pressure, followed by equilibration and (3) reentrant reequilibration using continuous decompression. In the continuous decompression scenario only 5 of the 9 reentrants from the Huckleberry Ridge could be modeled; the other 4 lacked plausible degassing paths from their inferred MI start.

Table 1. Sample localities for all reentrants used in this study

Eruption	Sample locality	Latitude/ Longitude	Samples collected or re-collected	Location description
Bishop	25	37.545386° N 118.592387° W	BTMM F2-5, F4-5	West side of Owens Gorge near Upper Power House penstocks. Thick section of F1 to F6. Capped by Ig1Eb ignimbrite.
Bishop	22	37.408818° N 118.493665° W	BTMM F7-1	Chalk Bluffs. Fall deposit stratigraphy present from F1-F9, with thick Ig2E ignimbrite on top.
Bishop	876	37.772230° N 118.519427° W	BTMM F8-2	Disused pumice pit in Blind Spring valley. Exposure of F7-F9 with interbedded IgE1b and capping Ig2E. Sampled 12-17 cm from F8/F9 contact, below the first appearance of Glass Mountain rhyolite lithics.
Bishop	764	37.518558° N 118.324267° W	BP138, BP141	Disused pumice pit on western slopes of the White Mountains. 2.1 meter-thick exposure of F9 with a thin (~1 cm) interbedded layer of Ig2Eb ignimbrite.
Oruanui	2288	38.656900° S 176.029402° E	Additional sample of the P1970 and P1971 layers	Punatekahi scoria quarry. Fall Phases 1-3 are present, with interbedded flow materials in phases 2 and 3. Phase 7 ignimbrite erosively overlies these units
Oruanui	2751	38.699660° S 175.999062° E	P1958-P1971 (same levels as used in Allan et al. 2012)	Natural exposure. Phases 1 to 3 present, with thin ignimbrite and other pyroclastic density current deposits interbedded with fall deposits of phases 2 and 3.
Oruanui	1086	38.882998° S 176.077834° E	P2305 whole pumices	Cut face alongside Hinemaiaia C dam. Coarser zone in Phase 3 ash-rich pyroclastic density current deposits sampled.
Huckleberry Ridge	5	44.974323° N 110.664595° W	MM3-MM11 YP287	Lower 1.8 meters of total 2.5 meter fine-grained fall deposit below thick, welded ignimbrite member A. See Myers et al. (2016) for sampling details.

DOI: https://doi.org/10.2138/am-2018-6225

Table 2. Summary description of the 31 reentrants analyzed in this study

Reentrant label	Eruption	Sample locality^	Fall layer†	Temp (° C)	Length of reentrant (μ m)	FTIR inner H_2O (wt.%)	FTIR inner CO_2 (ppm)	Interior pressure* (MPa)	Rim pressure* (MPa)
BT F2-5 RE #3	Bishop	25	F2	740	220	3.5	0	71	28
BT F2-5 RE #1	Bishop	25	F2	740	240	3.7	0	77	35
BT F4-5 RE #10	Bishop	25	F4	740	90	4	53	90	66
BT F4-5 RE #4	Bishop	25	F4	740	180	2.9	0	50	17
BTF7-1 RE #4	Bishop	22	F7	740	110	3.4	0	67	53
BTF7-1 RE #2	Bishop	22	F7	740	260	3.7	0	78	32
BTF8-2 RE #1	Bishop	876	F8	740	120	4.9	0	131	59
BTF8-2 RE #2	Bishop	876	F8	740	400	4.4	0	100	36
BTF9-2 RE #1	Bishop	876	F9	740	120	5.2	60	155	52
BTF9-2 RE #2	Bishop	876	F9	740	330	4.0	275	128	60
BTF9_138 RE #2	Bishop	764	F9	740	170	4.5	220	143	36
BTF9_141 RE #1	Bishop	764	F9	740	240	4.2	0	99	46
BTF9_141 RE #2	Bishop	764	F9	740	300	3.9	240	120	55
P1963-6 RE #1	Oruanui	2288	F1	780	220	1.9	100	38	13
P1968 BB2 RE #1	Oruanui	2288	F1	780	450	3.1	0	61	12
P1968-1 RE #5	Oruanui	2288	F1	780	240	3.5	90	88	32
P1970-A RE #6	Oruanui	2751	F2	780	160	3.5	100	89	54
P1971-3 RE #1	Oruanui	2751	F2	780	220	2.2	0	33	16
P1971-3 RE #2	Oruanui	2751	F2	780	140	2.5	25	45	25
P2305-D RE #1	Oruanui	1086	F3	780	270	3.9	0	92	50
P2305-E RE #1	Oruanui	1086	F3	780	310	4	0	96	51
P2305-F RE #1	Oruanui	1086	F3	780	310	3.3	0	68	50
MM11 RE #14	HRT	5	lower	800	110	2.1	210	60	22
MM10 RE #18	HRT	5	lower	800	170	3.3	250	106	33
MM10 RE #21	HRT	5	lower	800	150	3.4	50	81	30
MM7 RE #10	HRT	5	middle	800	120	2.6	180	71	25
MM7 RE #13	HRT	5	middle	800	230	2.1	205	59	36
MM5 RE #2	HRT	5	middle	800	140	3.1	450	127	71
MM4 RE #6	HRT	5	middle	800	225	2	445	89	46
MM4 RE #12	HRT	5	middle	800	195	2.1	400	85	40
MM4 RE #13	HRT	5	middle	800	180	2.9	300	98	66

Notes:
^Sample localities from Wilson and Hildreth (1997: Bishop), Wilson (2001: Oruanui) and Wilson (unpublished: Huckleberry Ridge).
†Fall deposit labels from Wilson and Hildreth (1997: Bishop) and Wilson (2001: Oruanui); see Myers et al. (2016) for MM sample levels.
*Calculated using H_2O and CO_2 solubility relationships from Volatilecalc (Newman and Lowenstern 2002).

DOI: https://doi.org/10.2138/am-2018-6225

(See separate file for Table 3.

DOI: https://doi.org/10.2138/am-2018-6225

Table 3. Starting conditions for and results from magma ascent modeling

	Starting MIs		Starting REs			Ascent based on reentrants						Ascent based on MIs					
Reentrant Name	Starting Pressure (MPa)*	MI H_2O Start (wt.%)	FTIR Inner H_2O (wt.%)	FTIR Inner CO_2 (ppm)	Starting Pressure (MPa)*	Ascent rate 1D Code MPa/s	d*P*/d*t* Error MPa	Bubble radius (μm)	Ascent time (hr)	Ascent Rate (m/s)	RE χ^2	Ascent rate 1D Code MPa/s	d*P*/dt Error MPa	Bubble radius (μm)	Ascent Time (hr)	Ascent rate (m/s)	MI χ^2
BT F2-5 RE #3	175	5.4	3.5	0	71	0.025	0.006	0	0.68	0.73	0.4	0.01	0.001	0	4.58	0.36	1.2
BT F2-5 RE #1	175	5.4	3.7	0	77	0.046	0.01	0	0.40	1.39	0.3	0.013	0.002	0	3.53	0.46	2.4
BT F4-5 RE #10	175	5.4	4	0	90	0.35	0.05	0	0.06	11.06	0.4	0.074	0.001	0	0.62	2.63	4.9
BT F4-5 RE #4	175	5.4	2.9	0	50	0.024	0.005	0	0.46	0.58	0.4	0.0084	0.003	0	5.46	0.30	0.8
BTF7-1 RE #4	175	5.4	3.4	0	67	0.16	0.07	0	0.10	4.57	0.2	0.044	0.01	0	1.04	1.56	2.0
BTF7-1 RE #2	175	5.4	3.7	0	78	0.02	0.005	0	0.94	0.61	0.1	0.006	0.0002	0	7.64	0.21	1.2
BTF8-2 RE #1	175	5.4	4.9	0	131	0.38	0.12	0	0.09	12.99	0.8	0.14	0.03	0	0.33	4.97	8.2
BTF8-2 RE #2	175	5.4	4.4	0	100	0.022	0.005	0	1.14	0.71	0.8	0.006	0.001	0	7.64	0.21	4.1
BTF9-2 RE #1	175	5.4	5.2	60	155	0.24	0.02	0	0.17	8.40	1.0	0.22	0.02	0	0.21	7.81	1.7
BTF9-2 RE #2	220	5.4	4.0	275	128	0.02	0.004	0	1.64	0.68	0.9	0.016	0.003	100	3.65	0.58	1.4
BTF9_138 RE #2	220	5.4	4.5	220	143	0.062	0.01	80	0.60	2.15	1.0	0.042	0.004	20	1.39	1.53	0.9
BTF9_141 RE #1	175	5.4	4.2	0	99	0.027	0.005	0	0.92	0.87	0.7	0.015	0.001	0	3.06	0.53	2.9
BTF9_141 RE #2	220	5.4	3.9	240	120	0.012	0.002	20	2.55	0.40	0.9	0.012	0.002	100	4.86	0.44	1.1
P1963-6 RE #1	190	5.0	1.9	100	38	0.0034	0.001	80	2.29	0.06	1.0	0.0028	0.001	120	17.86	0.10	4.6
P1968 BB2 RE #1	190	5.0	3.1	0	61	0.0072	0.001	0	1.97	0.20	1.0	0.0026	0.001	0	19.23	0.09	3.8
P1968-1 RE #5	190	5.0	3.5	90	88	0.042	0.003	20	0.52	1.32	0.6	0.014	0.004	0	3.57	0.50	1.3
P1970-A RE #6	190	5.0	3.5	100	89	0.11	0.01	0	0.20	3.47	1.0	0.034	0.007	0	1.47	1.22	1.2
P1971-3 RE #1	190	5.0	2.2	0	33	0.0052	0.002	0	1.23	0.07	0.1	0.003	0.002	0	16.67	0.11	0.1
P1971-3 RE #2	190	5.0	2.5	25	45	0.022	0.004	0	0.44	0.48	0.9	0.012	0.002	0	4.17	0.43	1.2
P2305-D RE #1	170	5.0	3.9	0	92	0.076	0.03	0	0.30	2.42	1.0	0.012	0.002	0	3.70	0.42	6.0
P2305-E RE #1	170	5.0	4	0	96	0.044	0.05	0	0.54	1.41	0.6	0.016	0.003	0	2.78	0.57	2.9
P2305-F RE #1	170	5.0	3.3	0	68	0.09	0.002	0	0.18	2.59	1.0	0.015	0.002	0	2.96	0.53	3.3
MM11 RE #14	200	4.7	2.1	210	60	0.014	0.002	10	0.99	0.38	0.6	0.012	0.001	40	4.40	0.43	0.5
MM10 RE #18	200	4.7	3.3	250	106	0.044	0.006	70	0.61	1.45	0.9	0.03	0.004	100	1.76	1.08	0.8
MM10 RE #21	200	4.7	3.4	50	81	0.054	0.003	80	0.37	1.65	0.5	0.026	0.006	100	2.03	0.94	1.2
MM7 RE #10	150	4.1	2.6	180	71	0.072	0.015	0	0.24	2.11	0.2	0.028	0.004	40	1.39	0.98	0.4
MM7 RE #13	150	4.1	2.1	205	59	0.033	0.01	40	0.41	0.88	0.2	0.0086	0.002	200	4.52	0.30	2.7
MM5 RE #2	210	3.9	3.1	450	127	0.059	0.02	0	0.55	2.01	0.4	0.064	0.01	0	0.87	2.31	1.3
MM4 RE #6	210	3.9	2	445	89	0.013	0.002	0	1.69	0.41	0.6	0.011	0.002	80	5.05	0.40	2.1
MM4 RE #12	210	3.9	2.1	400	85	0.009	0.002	0	2.31	0.28	0.3	0.007	0.002	120	7.94	0.25	0.6
MM4 RE #13	210	3.9	2.9	300	98	0.12	0.02	100	0.20	3.88	0.8	0.016	0.001	20	3.47	0.58	5.8

Notes: Two options are presented: (1) H_2O and CO_2 based on co-erupted melt inclusion concentrations (Myers 2017), and (2) based on concentrations measured from the interior of the reentrant. The chi-squared misfit between the modeled slope and measured data are given for each reentrant with both sets of starting conditions. Errors in analyses are as follows: Bishop – H_2O = 0.2 wt.%, CO_2 = 20 ppm; Oruanui phases 1 and 2 – H_2O = 0.2 wt.%, CO_2 = 30 ppm, Phase 3 – H_2O = 0.3 wt.%, CO_2 = 20 ppm; Huckleberry – H_2O = 0.3 wt.%, CO_2 = 30 ppm.

DOI: https://doi.org/10.2138/am-2018-6225

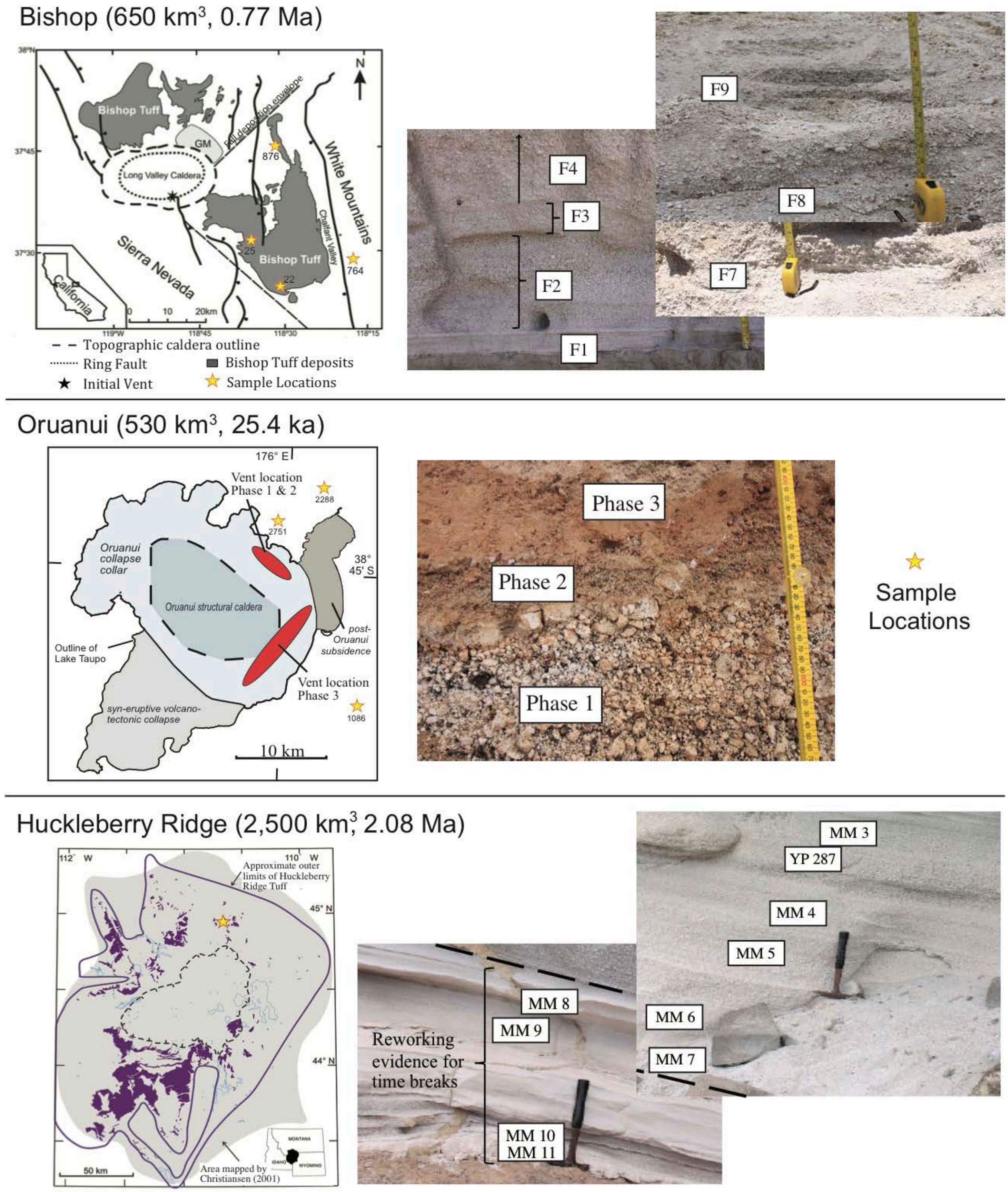

Myers et al. Figure 1

DOI: https://doi.org/10.2138/am-2018-6225

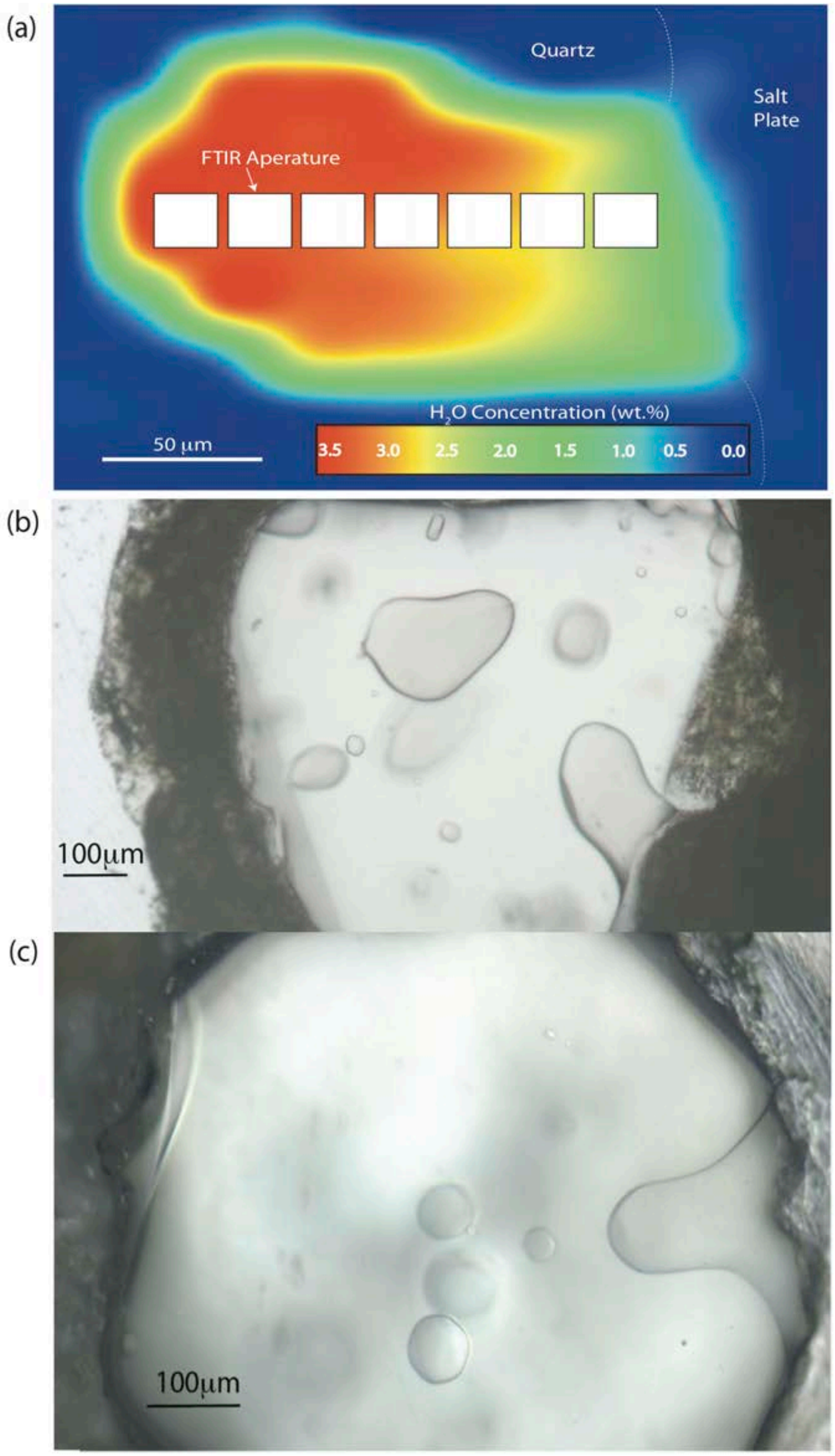

Myers et al. Figure 2

This is a preprint, the final version is subject to change, of the American Mineralogist (MSA)
Cite as Authors (Year) Title. American Mineralogist, in press.
DOI: https://doi.org/10.2138/am-2018-6225

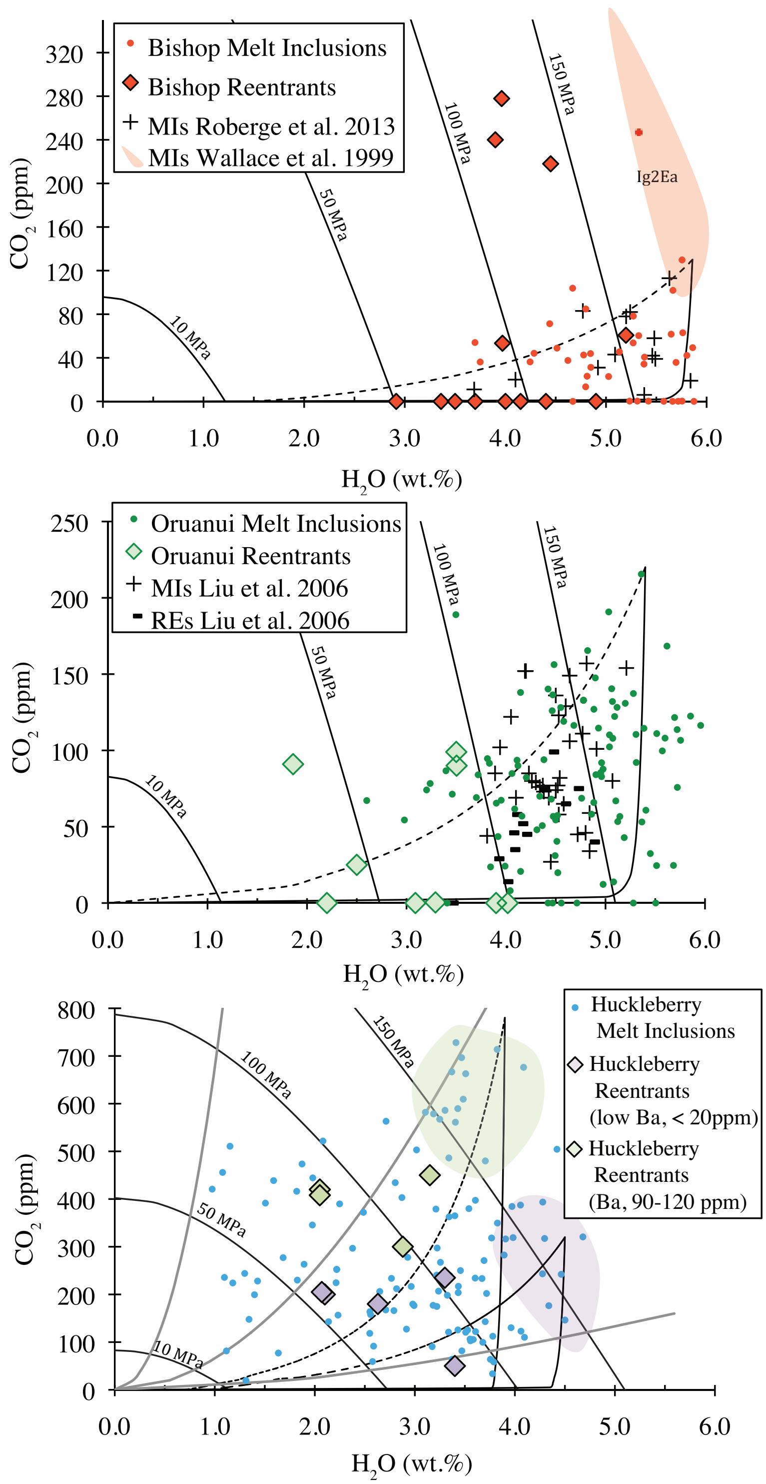

Myers et al. Figure 3

This is a preprint, the final version is subject to change, of the American Mineralogist (MSA)
Cite as Authors (Year) Title. American Mineralogist, in press.
DOI: https://doi.org/10.2138/am-2018-6225

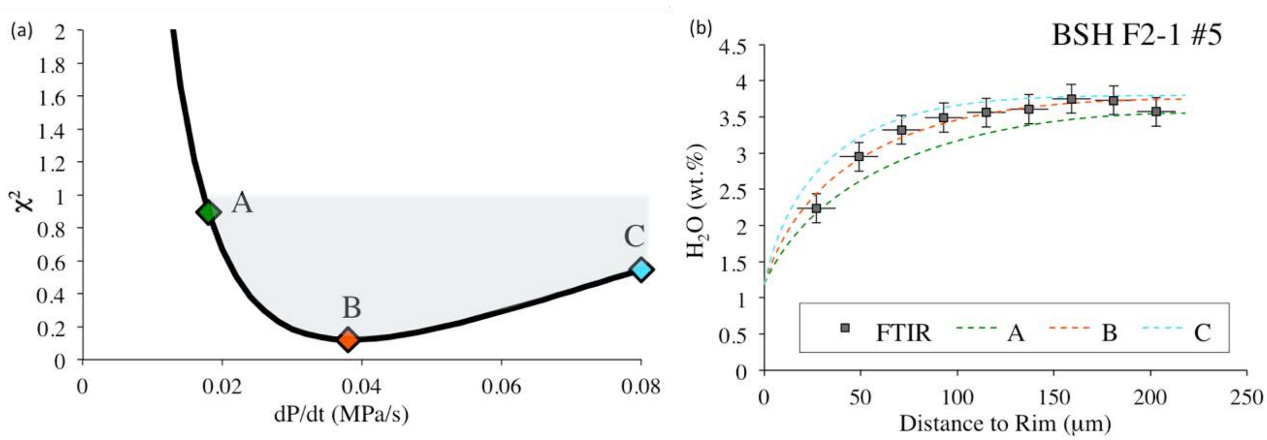

Myers et al. Figure 4

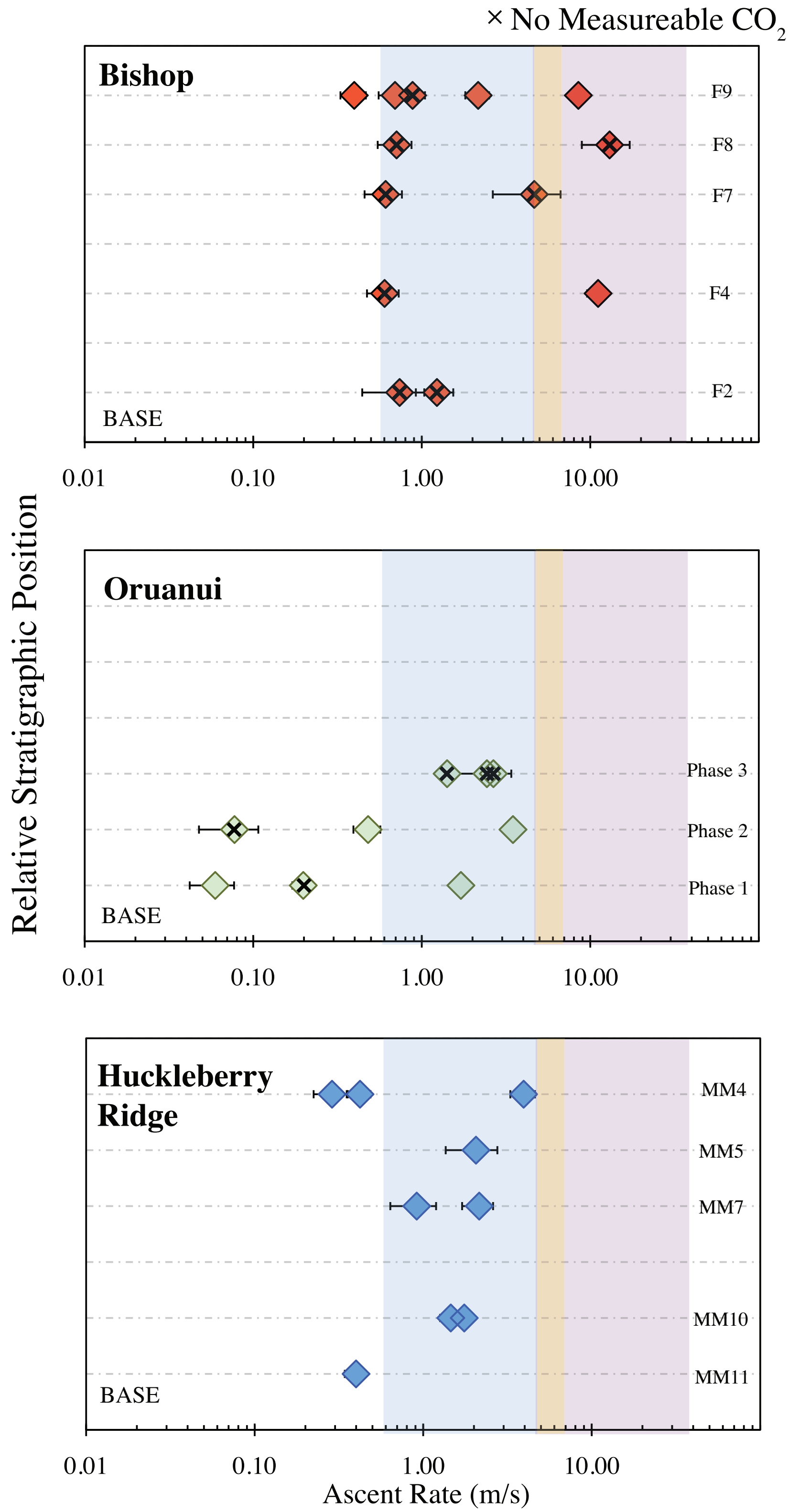

Myers et al. Figure 5

This is a preprint, the final version is subject to change, of the American Mineralogist (MSA)
Cite as Authors (Year) Title. American Mineralogist, in press.
DOI: https://doi.org/10.2138/am-2018-6225

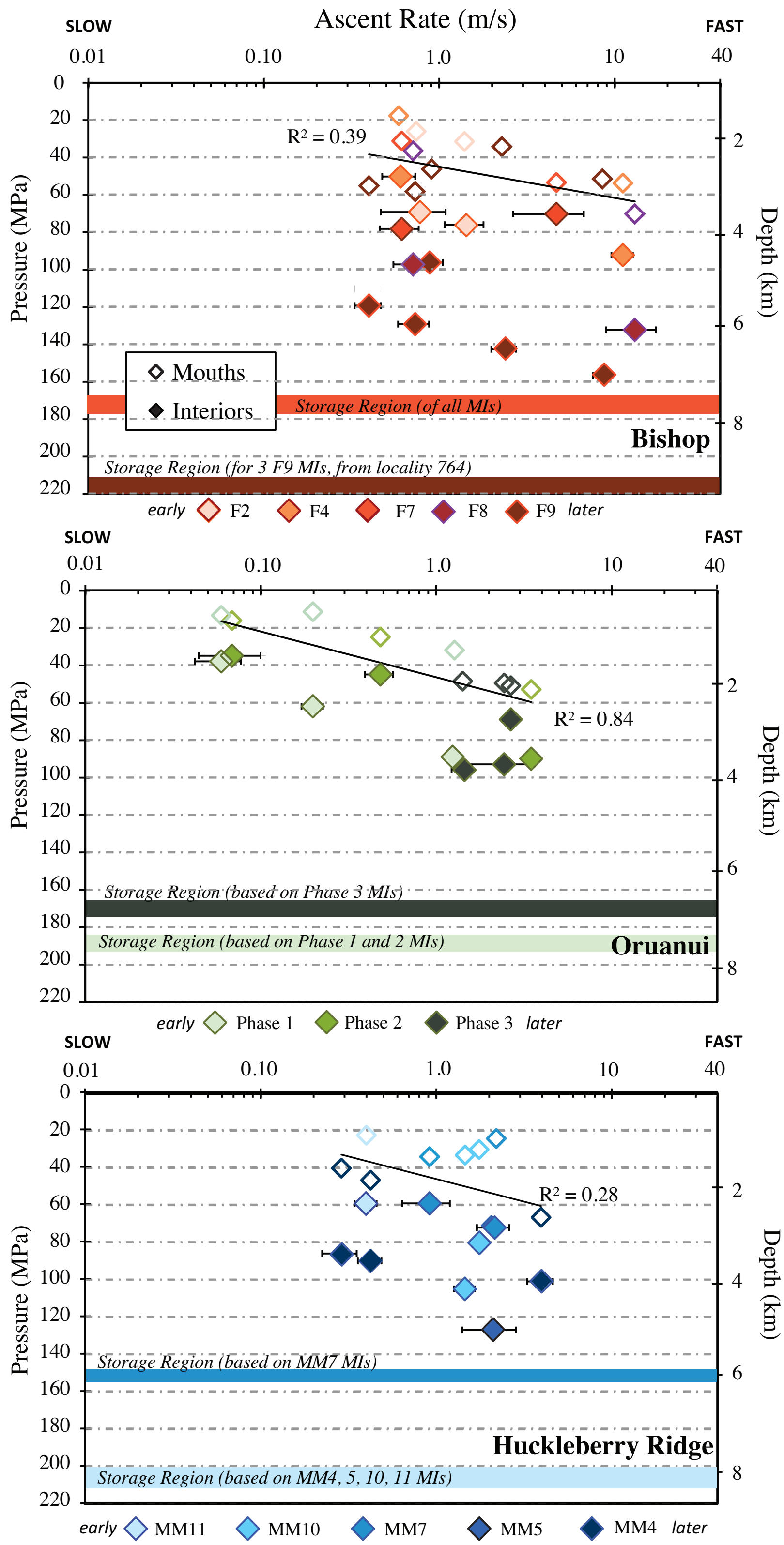

Myers et al. Figure 6

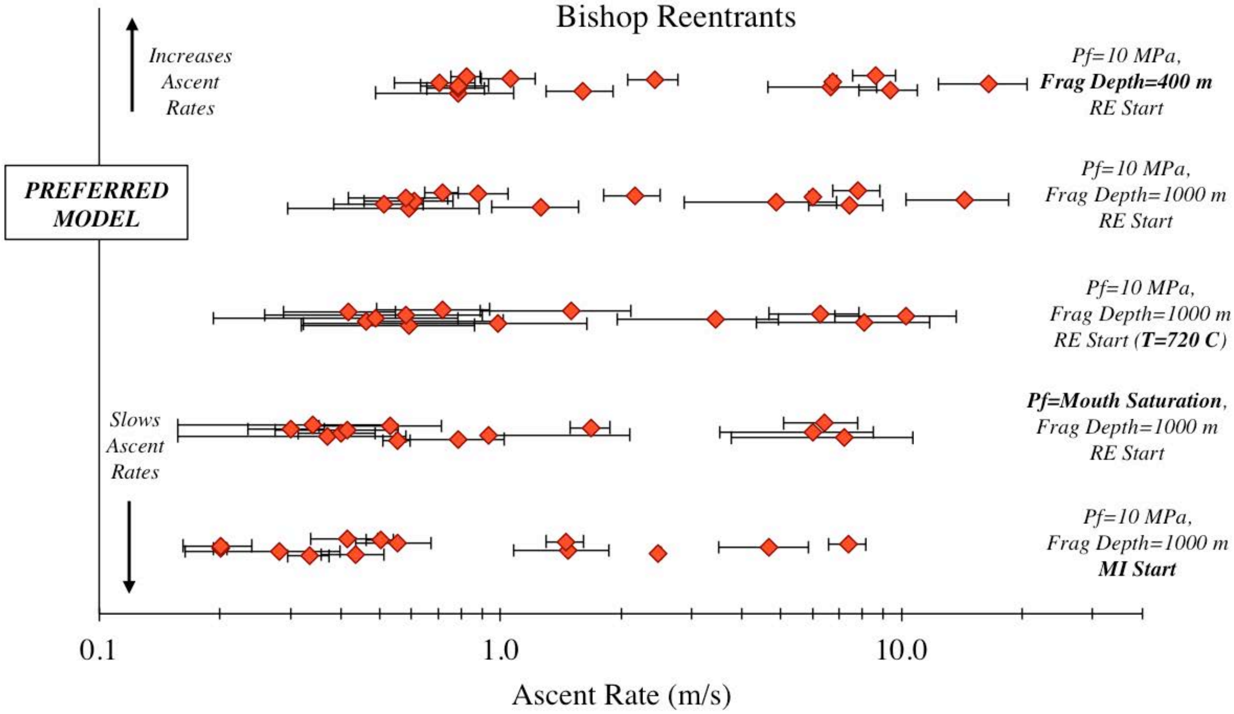

Myers et al. Figure 7

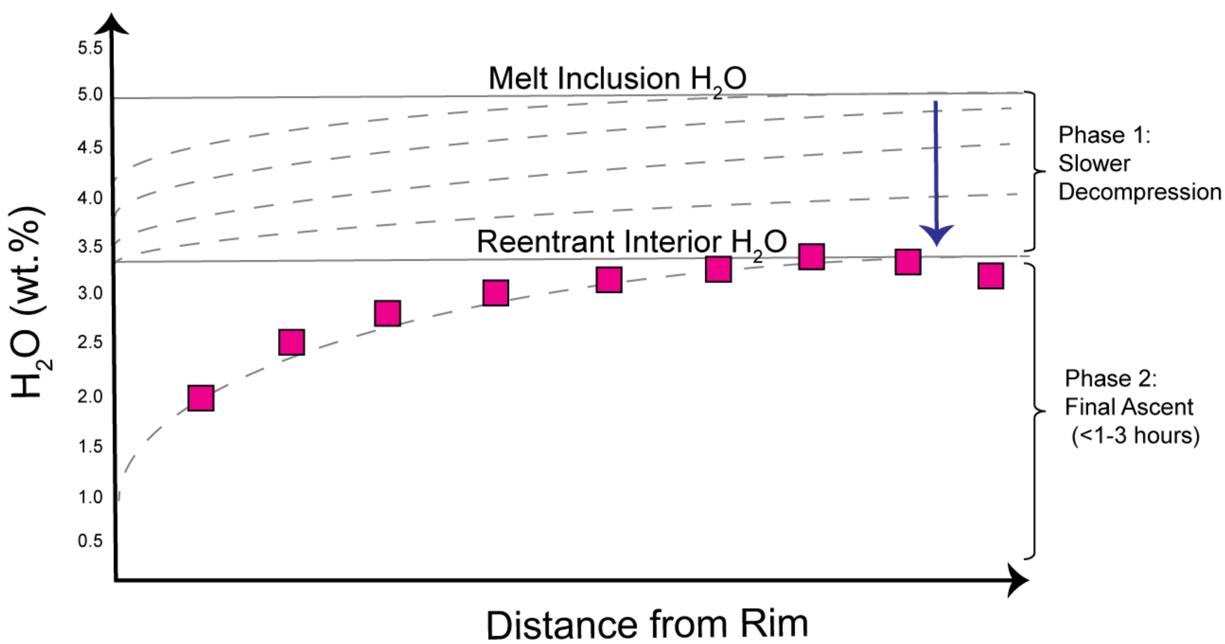

Myers et al. Figure 8

This is a preprint, the final version is subject to change, of the American Mineralogist (MSA)
Cite as Authors (Year) Title. American Mineralogist, in press.
DOI: https://doi.org/10.2138/am-2018-6225

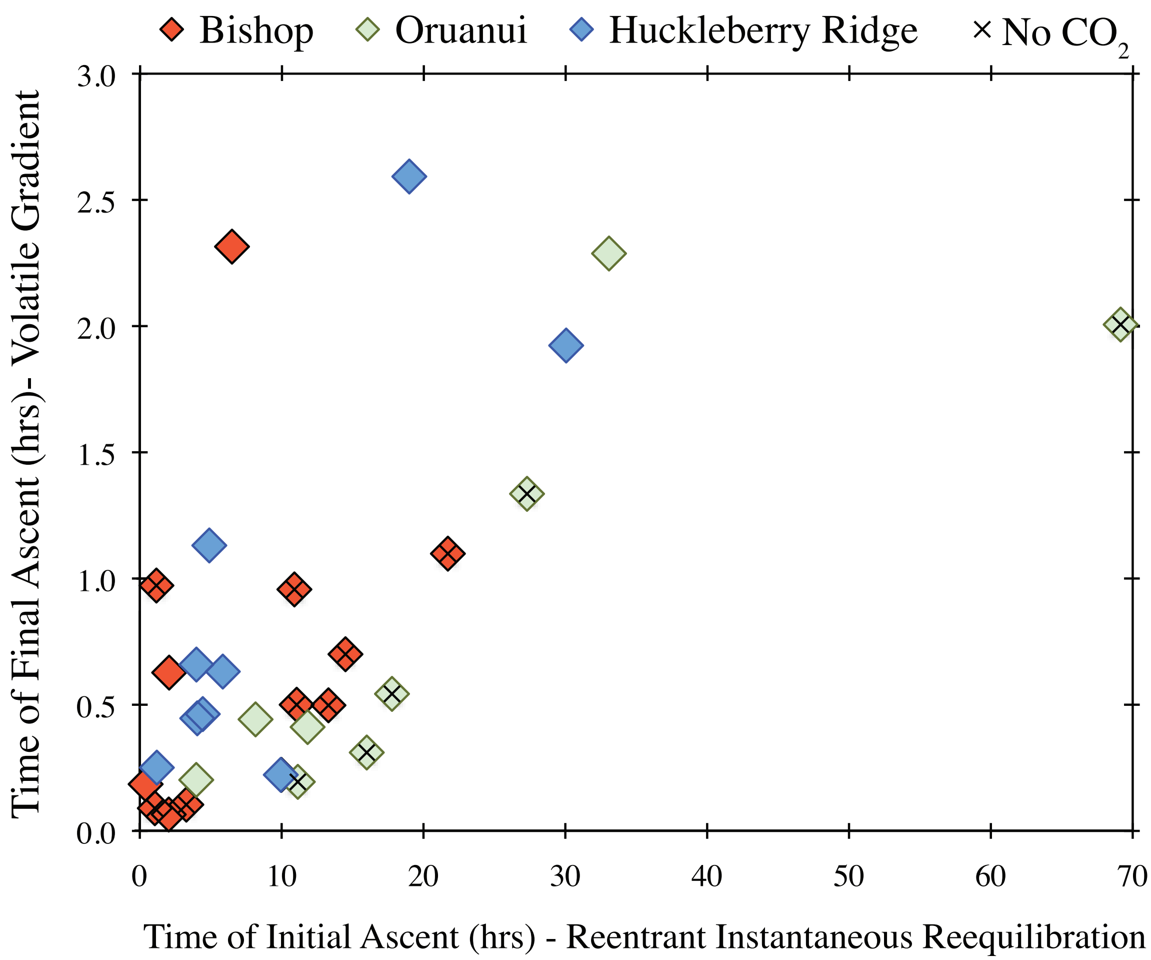

Myers et al. Figure 9

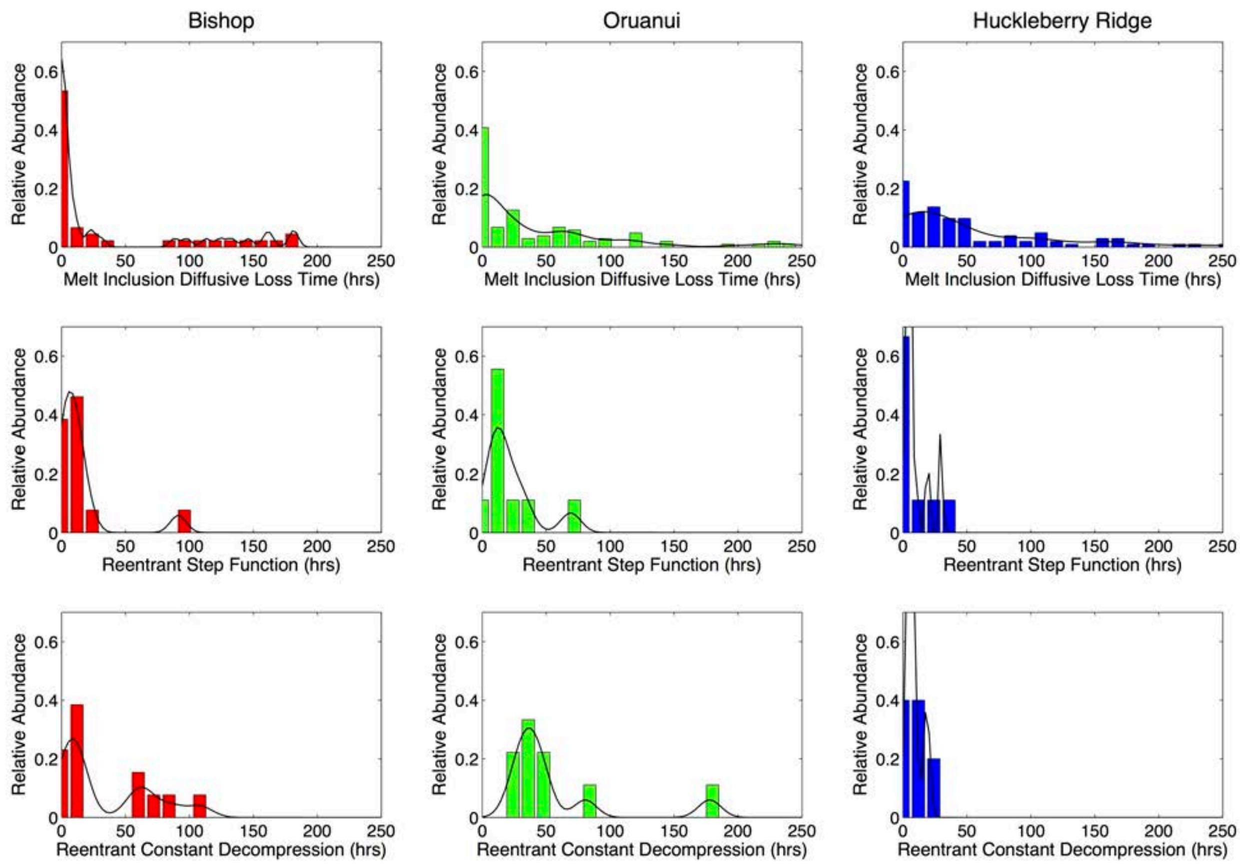

Myers et al. Figure 10